

# The seasonal cycle of upper-ocean mixing at 8°N in the Bay of Bengal

D. A. CHERIAN<sup>\*†</sup>, E. L. SHROYER

*College of Earth, Ocean, and Atmospheric Sciences, Oregon State University, Corvallis, Oregon, USA*

H. W. WIJESEKERA

*Naval Research Laboratory, Stennis Space Center, Mississippi, USA*

J. N. MOUM

*College of Earth, Ocean, and Atmospheric Sciences, Oregon State University, Corvallis, Oregon, USA*

## ABSTRACT

We describe the seasonal cycle of mixing in the top 30–100 m of the Bay of Bengal as observed by moored mixing meters ( $\chi$  pods) deployed along 8°N between 85.5°E and 88.5°E in 2014 and 2015. All  $\chi$  pod observations were combined to form seasonal-mean vertical profiles of turbulence diffusivity  $K_T$  in the top 100 m. The strongest turbulence is observed during the southwest and post-monsoon seasons i.e. between July and November. The northeast monsoon (December – February) is a period of similarly high mean  $K_T$  but an order of magnitude lower median  $K_T$ , a sign of energetic episodic mixing events forced by near-inertial shear events. The months of March and April, a period of weak wind forcing and low near-inertial shear amplitude, are characterized by near-molecular values of  $K_T$  in the thermocline for weeks at a time. Strong mixing events coincide with the passage of surface-forced downward-propagating near-inertial waves and with the presence of enhanced low-frequency shear associated with the Summer Monsoon Current and other mesoscale features between July and October. This seasonal cycle of mixing is consequential. We find that monthly-averaged turbulent transport of salt out of the salty Arabian Sea water between August and January is significant relative to local  $E - P$ . The magnitude of this salt flux is approximately that required to close model-based salt budgets for the upper Bay of Bengal.

## 1. Introduction

The Bay of Bengal (the Bay) is the eastern semi-enclosed basin of the north Indian Ocean. The shallow salinity-controlled stratification in the upper Bay allows for rapid coupling with the atmosphere, and modulation of sea surface temperature (SST) within the Bay of Bengal has been linked to variations in the South Asian monsoon (e.g., Vecchi and Harrison 2002; Roxy 2014). The influence of processes controlling upper ocean stratification thus extend beyond the physical footprint of the Bay. The Bay has a particularly strong influence on rainy and dry periods over the Indian subcontinent, termed active and break periods respectively. Much of central India’s annual rainfall results from convective systems that originate over the Bay and then propagate northwestward over the Indian subcontinent between June and September (Gadgil 2003; Goswami et al. 2003). Interannual variations in mean

rainfall are strongly correlated with fluctuations in India’s agricultural output (Gadgil and Rupa Kumar 2006), lending significant social relevance to the problem of understanding air-sea interaction and near-surface ocean dynamics that influence the Bay’s SST.

The Bay’s physical oceanography is characterized by two major features. First, its circulation reverses seasonally under the influence of the Indian Ocean monsoon — the seasonal reversal of winds north of approximately 10°S in the Indian Ocean basin. Second, it receives an immense amount of freshwater — more than 50% of the freshwater runoff into the entire tropical Indian ocean (Sengupta et al. 2006; Gordon et al. 2016).

The Indian Ocean monsoon and its associated precipitation is visualized in Figure C1 using seasonal mean wind stress from the Tropflux estimate (Kumar et al. 2012) and precipitation from the Tropical Rainfall Measuring Mission (TRMM) Multi-satellite Precipitation Analysis dataset (Huffman et al. 2007). Between May and September (southwest or SW monsoon), the winds are strong and southwesterly throughout the Indian Ocean basin. Pre-

<sup>\*</sup>Current affiliation: National Center for Atmospheric Research, Boulder, Colorado, USA.

<sup>†</sup>Corresponding author address: Deepak A. Cherian, NCAR, P.O. Box 3000, Boulder, CO 80307-3000.  
E-mail: deepak@cherian.net

precipitation over the Indian subcontinent is substantial (Figure C1c). The months of October and November (post-monsoon period, SWNE) are characterized by weak mean wind stress over most of the basin including the Bay (Figure C1d). Seasonal averaging hides the episodic presence of strong cyclones in the Bay that bring large amounts of rain and significantly affect lives of those residing along the perimeter of the Bay. Recent examples of cyclones that strengthened over the Bay and made landfall resulting in loss of life and severe damages, include Category 5 Tropical Cyclone Phailin in October 2013 and Category 4 Tropical Cyclone Hudhud in October 2014. The mean winds strengthen in December and switch to being northeasterly up until February (northeast or NE monsoon). These winds are weaker than those during the SW monsoon. Nations on the Bay's Rim i.e. India and Sri Lanka receive relatively little rainfall during this period and the precipitation maximum is located over the Bay (Figure C1a). The months of March and April are a period of weak winds and almost no precipitation north of 4°N (northeast-southwest transition, NESW; Figure C1b).

The monsoon imprints seasonality on the Bay's circulation (Schott et al. 2002; Shankar et al. 2002). The East India Coastal Current (EICC) spins up at the Bay's western boundary during both monsoons, flowing northward between May and October and then southward between December and April. The EICC is readily visible in seasonally-averaged estimates of near-surface ocean velocity (vectors in Figure C2a–e from the Ocean Surface Current Analysis Real-time product, OSCAR; Bonjean and Lagerloef 2002)<sup>1</sup> The EICC exists as a discontinuous flow with many recirculation loops and is visible as a local maximum along India's eastern coast in maps of geostrophic eddy kinetic energy  $EKE = 0.5[u_g^2 + v_g^2]$  (colored field in Figure C2a–e; Durand et al. 2009). Here  $(u_g, v_g)$  are geostrophic velocity anomalies computed from delayed-time sea surface height estimates as measured by multiple satellite altimeters by the Copernicus Marine Environment Monitoring Service (CMEMS)<sup>2</sup>. Apart from the EICC, one other major circulation feature is the Summer or Southwest Monsoon Current (SMC). The SMC is visible in the seasonal mean during the SW monsoon as an eastward jet along 8°N between 85°E and 92°E in Figure C2d (vectors). Peak velocity in the SMC can exceed  $1.5 \text{ m s}^{-1}$  and northward transport has been estimated to be in the range 10–27 Sv, likely an overestimate due to the presence of recirculations (Wijesekera et al. 2016; Vinayachandran et al. 1999; Webber et al. 2018). The southwestern and south-central Bay is a site of energetic

mesoscale variability during the SW monsoon (our Figure C2d; Chen et al. 2018). The elevated EKE reflects at least three mesoscale features: a westward propagating anticyclone (Wijesekera et al. 2016), a large cyclonic eddy that spins up annually off the coast of Sri Lanka (the Sri Lanka Dome, Vinayachandran and Yamagata 1998) and the SMC which threads a pathway between the Sri Lanka Dome to the north and the anticyclone to the south (Vinayachandran et al. 1999; Wijesekera et al. 2016). During the NE monsoon, the mean circulation in southern Bay reverses and the Northeast Monsoon Current flows westward with a weaker signal in EKE (Figure C2a,b).

Large outflows from the Ganga, Brahmaputra, and Irrawaddy rivers, and substantial precipitation make the Bay a strongly salinity-stratified basin in its near-surface depths particularly toward the north. The annual river discharge peaks towards the end of the SW monsoon and the fresh water is eventually exported out along the Bay's western and eastern margins (Sengupta et al. 2006). The exported water is saline with  $S \approx 34\text{--}35$  psu. Hence maintaining the Bay's long term salt balance requires both an inflow of salty water from outside the Bay and the upward turbulent transport of that imported salt so as to permanently modify the near-surface freshwater (Vinayachandran et al. 2013).

The western half of the north Indian Ocean, the Arabian Sea, is generally considered the source of the required salty water (for example, Jensen 2001), although recently SanchezFranks et al. (2019) used a multiyear model to argue that the original source of the salty water is the western equatorial Indian Ocean. Regardless of specific source, both observations and models agree that the SMC is the dominant pathway for salty water entering the Bay (Jensen 2001; Vinayachandran et al. 2013; Webber et al. 2018)<sup>3</sup>. The salty signature of the SMC is visible in maps of the depth of the 34.75 isohaline surface which shallows by 25 m or so in the southwestern Bay during the summer monsoon (Figure C2k–o; Murty et al. 1992; Vinayachandran et al. 2013). The shallow depth of the  $S = 35$  psu isohaline in the southwestern and south-central Bay relative to the northern Bay led Vinayachandran et al. (2013) to hypothesize that the southern Bay is a site of enhanced mixing and associated salt fluxes that may be an important contributor to the salt budget of the Bay. In agreement with this hypothesis, model studies have implicated vertical mixing as the primary mechanism for diluting the immense amount of fresh water the Bay receives during the southwest monsoon (Akhil et al. 2014; Benschila et al. 2014; Wilson and Riser 2016).

<sup>1</sup>OSCAR is a diagnostic estimate of near-surface velocity at five-day frequency that ignores local acceleration and nonlinearities but accounts for geostrophic, thermal wind and Ekman currents.

<sup>2</sup>DT all-sat-merged Global Ocean Gridded SSALTO/DUACS Sea Surface Height L4 product and derived variables (dataset-duacs-rep-global-merged-allsat-phy-14-v3).

<sup>3</sup>Recent observations and model simulations describe a second pathway a persistent subsurface inflow of salty water during the NE monsoon that exists as a superposition of frequent salty intrusion events that average out to a region of broad northward flow of high salinity water west of 85°E (Wijesekera et al. 2015; Jensen et al. 2016).

Here, we summarize year-long direct observations of turbulence at three moorings along 8°N in the south-central Bay (white dots in Figures C1, C2). We show that the seasonal cycle of winds and currents described above is imprinted on mixing in the Bay with near-molecular mixing during the quiet transition period giving way to elevated mixing during both monsoon periods primarily associated with near-inertial shear (Sections 3c, 4a). The observed seasonal cycle in mixing is likely significant for the Bay's salt budget as has been previously hypothesized (Section 4c). We find that the upward turbulent salt transport out of subsurface high salinity water at 8°N is comparable to freshwater gained through precipitation (less evaporation).

## 2. Observations

### a. $\chi$ pod

All presented turbulence quantities were obtained using  $\chi$ Pods: self-contained instruments each consisting of two fast-response FP-07 thermistors, a pitot-static tube for high-frequency speed measurements, a pressure sensor, a compass, and accelerometers (Moum and Nash 2009; Moum 2015). Refinement over many years has resulted in a system that can return records of turbulent temperature fluctuations for up to a year or more. The two thermistors on the  $\chi$ pod record temperature fluctuations at 100Hz. Temperature gradient spectra are computed using 1 second data intervals and are fit to the theoretical spectrum of Kraichnan (1968) in the viscous-convective range (Moum and Nash 2009). The Kraichnan spectrum is a function of two quantities: the turbulence dissipation rate of temperature variance  $\chi$  and the turbulence dissipation rate of kinetic energy  $\varepsilon$ , but the  $\chi$ Pods only record one quantity, temperature. The dependence on  $\varepsilon$  arises from the Batchelor (1959) wavenumber  $(\varepsilon/\nu k_T^2)^{1/4}$  which marks the end of the viscous-convective range. Since  $\chi$ pod thermistors do not resolve the Batchelor wavenumber typically (e.g. Lueck et al. 1977), fitting the Kraichnan spectrum requires specification of  $\varepsilon$ . In the absence of an independent estimate of  $\varepsilon$ , we assume that the turbulence diffusivities of temperature  $K_T^t = \chi/2/T_z^2$  and density  $K_\rho^t = \Gamma\varepsilon/N^2$  are equal with mixing efficiency  $\Gamma = 0.2$  for stratified turbulence (Osborn and Cox 1972; Osborn 1980; and Gregg et al. 2018 respectively). This yields a relationship between  $\chi$  and  $\varepsilon$ ,

$$\varepsilon = \frac{N^2 \chi}{2\Gamma T_z^2} \quad (1)$$

and a solution is obtained by fitting the spectrum through the iterative procedure described in Moum and Nash (2009). The buoyancy frequency  $N$  and vertical temperature gradient  $T_z$  are estimated using two CTD instruments deployed above and below the  $\chi$ pod. *In-situ* comparisons between  $\chi$ pod estimates and more “standard”

estimates from vertical microstructure profiles are favorable under stably-stratified sheared conditions (Perlin and Moum 2012; Pujiana et al. 2018). Total temperature and salt diffusivities  $K_T, K_S$ , heat flux  $J_q^t$  and salt flux  $J_s^t$  are estimated from a time series of  $\chi$  using

$$K_T = \kappa_T(S, T, P) + \frac{\chi/2}{T_z^2}, \quad (2a)$$

$$K_S = \kappa_s + \frac{\chi/2}{T_z^2}, \quad (2b)$$

$$J_q^t = -\rho_0 c_p K_T T_z, \quad (2c)$$

$$J_s^t = -\rho_0 K_S S_z; \quad (2d)$$

where  $\kappa_T, \kappa_s$  are the molecular diffusivity of temperature and salinity respectively, and  $T_z, S_z$  are background temperature and salinity gradients (usually obtained by differencing nearby CTDs on the moorings; subscript  $z$  indicates  $z$ -derivative). Again we have assumed that high Reynolds number geophysical turbulence mixes all scalars at the same rate so that the *turbulence* diffusivities of both temperature and salinity are equal i.e.  $(\chi/2)/T_z^2$ .

A challenge with analyzing  $\chi$ Pods deployed in the Bay's thermocline is the frequent occurrence of weakly turbulent and near-laminar flow for extended periods of time as has been recorded with microstructure measurements in the Aegean Sea (Gregg et al. 2012) and in the Arctic (Scheifele et al. 2018). Analyzing microstructure measurements in such environments is challenging given that the usual assumptions of isotropy, steadiness and homogeneity break down (Rohr et al. 1988; Itsweire et al. 1993; Gargett et al. 1984). In weakly turbulent environments, the  $\chi$ pod records “bit noise” when the turbulent temperature fluctuations are below the FP-07 sensor's detection threshold. We can account for such behaviour using knowledge of the circuit components involved (Appendix B). When the recorded temperature variance of an one second subset of data is within an arbitrary factor of 1.5 of the inferred noise variance of the sensor, we set  $\varepsilon$  to NaN and  $\chi$  to 0 resulting in total diffusivities  $K_T, K_S$  being set to molecular values  $\kappa_T, \kappa_S$  and the resulting fluxes  $J_q^t, J_s^t$  being that due to molecular diffusion (eqn. 2). We do so following Gregg et al. (2012) with the understanding that setting  $\chi$  to any non-zero value during such periods seems unjustifiable.

### b. The 2014-2015 Bay of Bengal deployment

As part of the U.S. Office of Naval Research's Air Sea Interaction Regional Initiative (ASIRI) and the Naval Research Laboratory's (NRL) Effects of Bay of Bengal Freshwater Flux on Indian Ocean Monsoon (EBoB) programmes a number of moored mixing meters ( $\chi$ Pods, Moum and Nash 2009) were deployed on moorings in the southwestern Bay. This paper focuses on three moorings deployed along 8°N east of Sri Lanka in late December

2013 (Figure C3a and Table C1). The  $\chi$  pods ended up at a variety of depths and returned data up to February 2015 (Table C1, Figure C3b–i and Wijesekera et al. 2016). Nearly all were predominantly in the main thermocline (Figure C3b–e) and sampled the high salinity water associated with the Summer Monsoon Current (SMC) during the summer monsoon (Figure C3f–i). This region experiences a significant seasonal cycle in near-surface velocity and mesoscale eddy kinetic energy (Figure C2a–e). The moorings were displaced by up to 50m (“blowdown”) by mesoscale features when present.

Two Teledyne RD Instruments ADCPs were deployed at the top of each mooring: an upward-looking Workhorse 300 kHz sampling every half hour in 2 m bins and a downward-looking Long Ranger 75 kHz sampling every hour in 8 m bins (further details are available in Wijesekera et al. 2016). A data gap in velocity coverage exists between the two ADCPs that is approximately 21 m wide. The shallower  $\chi$  pod was deployed within the blanking zone of the downward looking ADCP, so shear can be directly estimated only at the deeper  $\chi$  pod. We estimate shear by first linearly interpolating the velocities over the gap in depth, central differencing the interpolated velocity over three 8 m wide bins, and then reintroducing the gap. Each mooring contained more than fifteen temperature sensors of various kinds distributed between the buoy and 352 m below the buoy. Salinity coverage was coarser with four sensors deployed within a 50 m depth below the buoy and one sensor at 352 m (Wijesekera et al. 2016). Three of the four shallow salinity sensors were concentrated around the two  $\chi$  pods which were deployed 12 m and 32 m below the buoy.

### 3. Results

We now describe a seasonal cycle in thermocline turbulence that coincides with a seasonal cycle in thermocline shear. The seasonal variation in turbulence will be discussed along with the seasonal variation in the shear field, decomposed into three components as described below. Bursts in near-inertial shear will be linked back to surface winds using an approximate estimate of mixed-layer wind energy input obtained using a slab mixed layer model, also described below. First we introduce and rationalize our decomposition of the shear field.

#### a. Seasonal cycle in observed vertical shear

At all three moorings, *Eulerian* rotary spectra of vertical shear  $S_{\text{total}} = \sqrt{u_z^2 + v_z^2}$  at 152 m depth<sup>4</sup> are dominated by a broad peak at  $-f_0$  (40%–60% of sampled variance), narrow secondary peaks at  $-f_0 \pm \omega_{M_2}$  ( $\omega_{M_2}$  is the  $M_2$  tidal frequency, 5%–10% variance) and distributed variance at

frequencies less than 10 days reflecting meanders of the Summer Monsoon Current (20% variance). These spectra are presented in Figure C4a,c,e (clockwise in black, counterclockwise in red). The narrow peaks at  $-f_0 \pm \omega_{M_2}$  are a sign of vertical advection or pumping of near-inertial shear layers by the  $M_2$  tide which Doppler-shifts spectral energy from  $-f_0$  to  $-f_0 \pm \omega_{M_2}$  (Alford 2001). The effect of tidal pumping can be removed by estimating the spectra in isopycnal space (e.g. Alford et al. 2017). Given the sparse sampling in salinity, we instead estimate spectra in *isothermal* space. The peaks at  $f_0 \pm \omega_{M_2}$  are much less prominent at the  $T = 18^\circ\text{C}$  isotherm at all moorings (annual mean depth 150m; Figure C4b,d,f), leading us to interpret the near-tidal peaks in the Eulerian spectra (Figure C4a,c,e) as primarily being near-inertial shear that is Doppler shifted to near-tidal frequencies. Ideally we would interpret the  $\chi$  pod mixing estimates using a time series of isothermal shear that is filtered to isolate the low frequency and near-inertial components. It is not possible to obtain a gapless estimate of these filtered components given the gap in ADCP coverage. Instead we proceed by conducting our analysis in the Eulerian frame as follows.

We decompose the total vertical shear  $S_{\text{total}}$  by linearly interpolating over the sampling gap in the vertical and then using a second-order Butterworth filter applied forwards and backwards to split the shear time series into four components: (a) low-frequency shear  $S_{\text{low}}$  (lowpass with half power point 9 days), (b) near-inertial shear  $S_{\text{in}}$  (bandpass between half power points 7 days and 2 days respectively), (c) near-tidal shear (bandpass between half power points 15.3 hours and 10.4 hours<sup>5</sup>) and (d) a residual  $S_{\text{res}}$ . These frequency ranges are shaded in Figure C4. Given the previous discussion, we incorporate near tidal shear with  $S_{\text{in}}$ . The combined sum  $S_{\text{in+}}$  represents any shear associated with near-inertial waves, advection of near-inertial waves by the tide as well as any tidal shear.

Depth-time maps of the mean squared shear for three shear components  $S_{\text{low}}$ ,  $S_{\text{in+}}$ ,  $S_{\text{res}}$  along with the total shear  $S_{\text{total}}$  are shown in Figure C5 (normalized by the temperature contribution to stratification  $N_z^2$ ). At all three moorings, energetic shear is observed in January, February, and for an extended period between July and November. The shear field is relatively weak between mid-March and the beginning of June. Episodic energetic bursts in near-inertial shear are seen at all three moorings outside these months. All three moorings see a large rise in low-frequency shear between July and November. This is an indication of the Sri Lanka Dome and a large anticyclonic eddy through the array as the meandering of the Summer Monsoon Current (note EKE maximum inferred from altimetric data in Figure C2a–e). The magnitude of the low-frequency shear is comparable to that of near-inertial shear

<sup>4</sup>We choose 152 m to avoid any uncertainties associated with interpolating over the gap in ADCP coverage.

<sup>5</sup> $0.95(\omega_{M_2} - f_0)$  to  $1.05(\omega_{M_2} + f_0)$

at all three locations during the SW monsoon. The residual  $S_{\text{res}}$  is generally weak relative to the  $S_{\text{low}}$  and  $S_{\text{in+}}$ . The episodic nature of near-inertial shear events prevent a confident estimation of the magnitude of its seasonal cycle given that only one full annual cycle was recorded. However the seasonal signal in *total* shear high shear between June and February, and low shear between March and June is robust and consistent across all three moorings.

### b. Seasonal cycle in near-inertial energy input

We provide context for the observed near-inertial shear events by using a slab mixed layer model to estimate wind-forced energy input  $\Pi$  in to the mixed layer. We follow Alford (2003) and obtain a slab model estimate of  $\Pi$ ,  $\Pi_{\text{slab}}$ , by forcing a slab ocean mixed layer model with reanalysis 10-m winds at hourly frequency (MERRA-2, the Modern-Era Retrospective Analysis for Research and Applications, Version 2, Gelaro et al. 2017) and using climatological monthly mixed layer depths from the Monthly Isopycnal Upper-Ocean Climatology with Mixed Layers dataset (MIMOC, Schmidtko et al. 2013). Details of the solution are described in Appendix A.

The SW monsoon winds drive moderate near-inertial flux nearly uniform throughout the Bay (Figure C2f–j). The largest near-inertial fluxes over the year are confined to latitudes south of 10°N until the months of October and November when strong input associated with the passage of Tropical Cyclone Hudhud (October 5–14, 2014) occurs between 12°N and 16°N. Intense near-inertial input in the Bay is forced by the passage of cyclonic systems as in the mid-latitudes (Alford 2003) — the tracks of Very Severe Cyclonic Storm Madi (December 7–11, 2013) and Depression BOB01 (January 2–6, 2014) are readily visible in the near-inertial input field for the NE monsoon. There is little to no near-inertial energy flux into the mixed layer during March (northern Bay) and April (entire Bay).

### c. Seasonal cycle in mixing

We illustrate the seasonal cycle of turbulence in two ways: (a) by first presenting a time series of daily-averaged observations at a single mooring (NRL5, Figure C6), and (b) by presenting a seasonally averaged vertical profile of diffusivity that synthesizes observations from all three moorings (Figure C7).

#### A PROTOTYPICAL TIME SERIES (NRL5; 8°N, 88.5°E)

We present the seasonal cycle of winds, turbulence, shear and stratification at mooring NRL5 using daily averaged quantities in Figure C6. We choose to highlight mooring

NRL5 for two reasons. First, it experiences the least blow-down and is least contaminated by the associated space-time aliasing (10–20 m, Figure C6f). Second, the turbulence quantities in Figure C6 are inferred from measurements recorded by the deep  $\chi$ pod at 105 m. This instrument is the deepest deployed in the Bay to date, and recorded the longest period of weak turbulence observed during the transition months of March and April. The filtered shear components shown in Figure C6d are obtained by first subsampling the filtered depth-time fields along the  $\chi$ pod's trajectory and then normalizing by 30-day lowpass filtered  $N^2$ . Time series recorded at the other moorings are presented in the Supplementary Material.

Mixing events during the NE monsoon are episodic and relatively weak ( $K_T \leq 10^{-6} \text{ m}^2 \text{ s}^{-1}$ ) while the transition months of March and April are a period of extremely weak mixing. The  $\chi$ pod measures sustained and relatively high mixing between the months of May and October — a period of energetic mesoscale activity and moderately large near-inertial energy input  $\Pi$  in the south-central Bay (Figures C2). The Summer Monsoon Current arrived at NRL5 in July, bringing in high salinity water and reducing  $N^2$  (Figure C6d). Its arrival coincided with the rise of  $K_T$  to sustained values greater than  $10^{-6} \text{ m}^2 \text{ s}^{-1}$ . However  $K_T$  was still consistently below and rarely exceeded the canonical mid-latitude thermocline value of  $10^{-5} \text{ m}^2 \text{ s}^{-1}$  ( $50\kappa_T$ , Figure C6b). Heat flux  $J'_q$  is likewise small and exceeds  $10 \text{ W m}^{-2}$  for only a few days in the entire year (Figure C6c).

#### A SEASONALLY VARYING VERTICAL PROFILE OF DIFFUSIVITY $K_T$

We synthesize all  $\chi$ pod observations along 8°N by constructing approximate seasonally-averaged vertical profiles of  $K_T$ , presented in Figure C7, as follows:

1. We label every averaged  $K_T$  measurement with the density value of the parcel as well as the depth of measurement.
2. All measurements are then binned by density with bin edges [1018, 1021, 1022, 1022.5, 1023, 1023.5, 1024.25, 1029]  $\text{kg m}^{-3}$ .
3. For each season, we construct a PDF of  $K_T$  in each bin and calculate the mean and standard deviation of the depths of measurement.
4. The PDFs are presented at the mean depth of the density bin as a vertical profile (Figure C7). Each PDF is labelled with the mean density in each bin; means and medians are marked by circles and diamonds respectively (see caption).

Some considerations must be kept in mind while interpreting Figure C7. First, our definition of seasons need

not line up perfectly with periods of relatively high or relatively low winds or mixing at every mooring. Second, the  $\chi$  pods on the NRL3 mooring appear to be within the mixed layer and the isothermal but salinity-stratified barrier layer for a few weeks in February. These measurements are excluded since we do not have enough observations to construct meaningful averages for the mixed and barrier layers. Third, Figure C7 ignores all spatial variability.

Despite these caveats, Figure C7 presents a useful summary of observed mixing along 8°N. There is a clear seasonal cycle in turbulent diffusivity in the upper 30–100m at all mooring locations that mirrors the seasonal cycle at NRL5 in Figure C6. Vertical profiles of both mean and median values of  $K_T$  are always surface intensified (tables of both means and medians are provided in Appendix B). The amplitude of the seasonal cycle in mean diffusivities is roughly an order of magnitude with mean  $K_T \approx 10^{-4} \text{ m}^2 \text{ s}^{-1}$  during both monsoons. Median  $K_T$  is approximately an order of magnitude larger during the SW monsoon as compared to the NE monsoon ( $10^{-6} \text{ m}^2 \text{ s}^{-1}$  versus  $10^{-7} \text{ m}^2 \text{ s}^{-1}$ ) indicating that energetic mixing events are rarer during the NE monsoon. The most striking feature of Figure C7 is the near-complete lack of mixing in the south-central Bay’s thermocline during the months of March and April — median diffusivity values are only slightly greater than molecular diffusivity  $\kappa_T$  at depths greater than 60 m. The observation of near-molecular diffusivity at the deep  $\chi$  pod at NRL5 is thus consistent across the other two moorings.

## 4. Discussion

### a. A seasonal cycle in shear and turbulence

We now describe the seasonal cycle of shear and turbulence by synthesizing Figures C5, C6 and C7.

#### NE MONSOON (DECEMBER – FEBRUARY)

During the NE monsoon, mean  $K_T \geq 10^{-5} \text{ m}^2 \text{ s}^{-1}$  ( $50\kappa_T$ ) and medians are lower by one to two orders of magnitude across all three moorings (Figure C7). All three ADCPs recorded the passage of energetic packets of near-inertial energy in January and February (Figure C5 and C6e). These packets are likely associated with the passage of Cyclonic Storm Madi and Depression BOB01, whose tracks are visible in the near-inertial input  $\Pi_{\text{slab}}$  (Figure C2f). Between December and February, the deep  $\chi$  pod at NRL5 records relatively weak turbulence with maximum  $K_T \approx 10^{-6} \text{ m}^2 \text{ s}^{-1}$ . Note that the near-inertial event is weakest at NRL5, Figure C5i.

#### TRANSITION (MARCH – APRIL)

Arguably our most dramatic observation is that the  $\chi$  pod at 105-m recorded near-laminar flow i.e. near-molecular values of  $K_T$  in the thermocline during the *entire* month of April. Similar periods of low to negligible mixing are present at other  $\chi$  pods, but for shorter periods of time. Median  $K_T \leq 10^{-6} \text{ m}^2 \text{ s}^{-1} \approx 5\kappa_T$  in most thermocline density bins (deeper distributions in Figure C7), so the observation of weak to negligible mixing is consistent across all locations. The transition months of March and April are a period of weak thermocline currents, weak thermocline shear, weak winds, high net surface heat flux and low near-inertial energy flux (Figures C2, C5 and C6). These conditions are consistent with the observations of weak mixing. Weak pulses of near-inertial shear are seen in Figures C5 and C6e; again this is consistent with weak wind forcing at the surface (Figure C2k–o). Stratification is relatively high at all  $\chi$  pod depths:  $N^2 \sim 5 \times 10^{-4} \text{ s}^{-2}$ .

#### SW MONSOON (MAY – SEPTEMBER)

With the onset of the SW monsoon, the  $\chi$  pods observe an order of magnitude increase in mean *thermocline* diffusivity to  $K_T \approx 10^{-4} \text{ m}^2 \text{ s}^{-1}$  ( $500\kappa_T$ ) with peak values of  $K_T \approx 10^{-2} \text{ m}^2 \text{ s}^{-1}$  ( $5 \times 10^4 \kappa_T$ ) between July and September (Figure C7). The mean diffusivity is two to four orders of magnitude larger than values observed during March and April (Figure C7). Median thermocline diffusivities during the SW monsoon are larger relative to the NE monsoon by a factor of 5 – 10 (Figure C7 and Table B2). The medians are also closer to the means during the SW monsoon (Figure C7), as compared to the NE monsoon, an indication of frequent energetic mixing events.

The SMC and other mesoscale features are visible in  $S_{\text{low}}$  at all three moorings during this season though for differing lengths of time (Figure C5). Both seasonal mean surface velocities from the OSCAR product and mooring ADCP data show the mesoscale to be prominent especially at NRL3 and NRL4, the two westernmost moorings along 8°N (also see Figures C2a–e, C8 and Wijesekera et al. 2016). This inference is consistent with the ADCP measurements (Figure C5). At NRL5, elevated mixing occasionally lines up with short periods of elevated low frequency shear between May and October (Figure C6e).

A few high mixing events are also associated with bursts of elevated near-inertial shear that last for one to two weeks at a time at NRL5 (Figure C6e). The maximum observed diffusivity and turbulence fluxes in Figure C6 coincide with the passage of a particularly strong set of near-inertial wave packets that forced enhanced turbulence at the  $\chi$  pod’s depth (July 25 – August 7, highlighted in white in Figure C6b,c). Zonal shear and  $K_T$  for this period of intense mixing are shown in Figure C9. The elevated mixing coincides with the passage of a set of  $M_2$  tide packets that

vertically displace the isotherms and the near-inertial shear in Figure C9b. The effect of tidal vertical advection can be removed by interpolating to isothermal or isopycnal space (Alford 2001). We first interpolate total shear to isothermal space and then filter to isolate the near-tidal and near-inertial bands. Squared near-inertial shear is larger than near-tidal shear on both isotherms by nearly an order of magnitude (Figure C9c). Vertical advection by the  $M_2$  tide is Doppler shifting energy to frequencies  $\approx -f_0 \pm \omega_{M_2}$  in Eulerian spectra (Figure C4). Hence we interpret the apparent modulation of  $K_T$  at near- $M_2$  frequency (Figure C9a) as a result of the  $M_2$  tide heaving near-inertial shear layers past the  $\chi$ pod, and not mixing forced by tidal shear.

#### POST-MONSOON (OCTOBER – NOVEMBER)

Energetic turbulence is observed at the NRL3 and NRL4 moorings during October and November (see  $\rho - 1000 = 22.2, 22.8$  and  $23.2 \text{ kg m}^{-3}$  bins in Figure C7). Surface velocities in the OSCAR dataset suggest that the SMC ceases to exist as a continuous inflow through the Bay's southern boundary at the end of September. Subsequent periods of enhanced low frequency shear in Figure C6e between October and January appear to be associated with westward propagating features seen in OSCAR surface velocity data (Figure C8). At NRL3, energetic mixing is recorded by the shallower  $\chi$ pod during October; unfortunately the gap in ADCP coverage prevents us from attributing this turbulence to a specific shear event. At NRL4 the  $\chi$ Pods record high mixing during November; again this coincides with a downward propagating near-inertial wave (Figure C5h). There are two strong wind events at the surface in October and November (Figure C6a) that are likely responsible for downward propagating near-inertial energy during this season (Figures C5; also see enhanced  $\Pi_{\text{slab}}$  in Figure C2f–j). At NRL5, there appears to be some mixing associated with a low-frequency shear peak in October (Figure C6b,e).

Despite the above noted tendency, near-inertial shear did not always correspond with high mixing. For example, negligible mixing is associated with a burst in near-inertial shear in November (Figure C6b,e). This wave packet appears to have forced turbulence at a depth not sampled by the  $\chi$ Pods, if at all. Enhanced near-inertial shear need not necessarily lead to mixing. Alford and Gregg (2001) observe that peak mixing associated with a downward propagating near-inertial wave occurs at the stratification maximum. As they point out, the presence of strong mixing at the stratification maximum is consistent with WKB scaling: the Froude number scales with stratification  $\text{Fr} = S/N \sim N^{1/4}$  so shear instability is expected where  $N$  is large. A  $\chi$ pod would need to be recording at the right depth relative to the stratification structure to observe turbulence forced by near-inertial energy — a major caveat to our analysis.

#### SUMMARY

There is a strong seasonal cycle in thermocline mixing (Figure C7) that appears to be linked to a seasonal cycle in thermocline shear (Figure C5). The seasonal cycle in shear results from (a) the seasonal presence of the Summer Monsoon Current which greatly increases low-frequency shear  $S_{\text{low}}$  between July and October, and (b) episodic energetic downward propagating near-inertial waves observed outside March and April. At times,  $S_{\text{low}}$  is of comparable magnitude to near-inertial shear  $S_{\text{in+}}$  (Figure C5). The seasonal cycle in low-frequency shear is expected from the well established seasonal spinup and spindown of the SMC and the Sri Lanka Dome (Schott and McCreary 2001; Vinayachandran and Yamagata 1998). A seasonal cycle in near-inertial shear is perhaps expected from the seasonal cycle of winds. However our ADCP record cannot sufficiently characterize the magnitude of the seasonal cycle in near-inertial energy, given the small number of large magnitude near-inertial events at all three moorings (Figure C5).

#### b. Weak turbulence in April

The  $\chi$ pod observations of near-molecular diffusivity values in April is consistent with previous *in-situ* finestructure- and microstructure-based profiles of turbulence quantities in the Bay. For example, Jinadasa et al. (2016) report vertical profiles of  $N^2 \approx 10^{-3} \text{ s}^{-2}$  and  $\varepsilon \geq 10^{-9} \text{ W kg}^{-1}$  from which we infer minimum diffusivity  $K_\rho^{\text{min}} = \Gamma_\varepsilon^{\text{min}}/N^2 \approx 2 \times 10^{-7} \text{ m}^2 \text{ s}^{-1} \approx \kappa_T$  at  $87^\circ\text{E}, 16^\circ\text{N}$ , 30 m (their Figure 2). Similarly St. Laurent and Merrifield (2017) also infer  $K_\rho \approx 10^{-6} \text{ m}^2 \text{ s}^{-1} (5\kappa_T)$  for depths between 40m and 120m by combining a mean vertical profile of  $\varepsilon$  and mean  $N$  collected by glider-based sensors over seven days. Their mean profile of  $\varepsilon$  shows  $\varepsilon \geq 10^{-9} \text{ W kg}^{-1}$  in the top 120 m. Lucas et al. (2016) infer  $K_T \leq 10^{-6} \text{ m}^2 \text{ s}^{-1}$  for depths deeper than 40 m using a  $\chi$ pod sensor on a vertical profiling platform (Wirewalker, Pinkel et al. 2011). Finally finestructure estimates of dissipation estimated using LADCP shear profiles for the GO-SHIP<sup>6</sup> I01 section at approximately  $10^\circ\text{N}$  in the Bay of Bengal yield  $K_\rho \approx 10^{-6} \text{ m}^2 \text{ s}^{-1} (5\kappa_T; \text{Kunze et al. 2006})$ .

A non-dimensional parameter that characterizes the transition from laminar to turbulent flow is the buoyancy Reynolds number  $\text{Re}_b = \varepsilon/(vN^2)$  (for example Itsweire et al. 1993). When  $\varepsilon \approx 10^{-9} \text{ W kg}^{-1}$ ,  $N^2 \approx 10^{-3} \text{ s}^{-2}$  (Jinadasa et al. 2016; St. Laurent and Merrifield 2017) and molecular viscosity  $\nu \approx 10^{-6} \text{ m}^2 \text{ s}^{-1}$ ,  $\text{Re}_b \approx 1$ . At such low values of  $\text{Re}_b$ , overturning turbulence ceases to exist and total diffusivity asymptotes to  $\kappa_T$  in direct numerical simulations as well as experiments (for e.g. Ivey et al.

<sup>6</sup>Global Ship-based Hydrographic Investigations Program

2008, their Figure 2; Itsweire et al. 1993). The microstructure  $\epsilon$  measurements of Jinadasa et al. (2016) and St. Laurent and Merrifield (2017) then independently indicate that weakly turbulent flows with near-molecular diffusivities are present in the Bay.

Low thermocline diffusivities are predicted by the finestructure internal-wave scaling of Henyey et al. (1986) and have been observed previously at low latitudes in the Pacific and Atlantic:  $K_\rho \approx (1-3) \times 10^{-6} \text{ m}^2 \text{ s}^{-1} (5 - 15 \kappa_T)$  for latitudes south of  $10^\circ\text{N}$  in Gregg et al. (2003). Our lowest observed values during March, April at approximately 80–100 m depths are frequently lower than those observations (Figures C7 and C6b). The extended period of low  $K_T$  values is perhaps unsurprising given the observations summarized above and that the transition months of March and April are a period of very low wind energy input i.e. weak inertial shear; weak mean flows i.e. weak low frequency shear; and considerable stratification (note low  $S^2/N^2$  in Figure C5). However these  $\chi_{\text{pod}}$  observations are the first to show that extremely low mixing ( $K_T \leq 1-10\kappa_T$ ) persists for multiple weeks at multiple locations in the south-central Bay (Figures C6b and C7).

It is possible that an inability to represent the observed low values of mixing has consequences for simulations of the Indian Ocean. Wilson and Riser (2016) find that “negative salinity biases at 50-m depth are associated with positive salinity biases near the surface” between February and May in an assimilative HYCOM simulation of the Bay. They then suggest that “the model is overestimating the strength of vertical mixing in the upper bay for those months and possibly for other times of the year.” This February to May time period is precisely when the  $\chi_{\text{pods}}$  observe very little mixing in the southern Bay (Figure C7). Furthermore, improved upper ocean state representation in the CFSv2 operational forecast model run by the Indian Institute of Tropical Meteorology for India’s Monsoon Mission programme has been shown to improve rainfall forecasts over central India (Koul et al. 2018). Chowdary et al. (2016) show this model to be biased cold in the top 80m, biased warm below 100m, excessively saline in the top 500 m and have excessive vertical turbulent heat fluxes in the top 200 m (*annual mean*). They link the high mixing bias to excess shear and reduced stratification in the model. Climate model configurations that account for the latitudinal variation of internal wave diffusivity noted in Gregg et al. (2003)<sup>7</sup> use a background  $K_T \approx (1-1.7) \times 10^{-5} \text{ m}^2 \text{ s}^{-1} (50\kappa_T)$  in the Bay (Danabasoglu et al. 2012; their Figure 1). This value is an order of magnitude larger than the mean  $K_T \approx (1-3)\kappa_T$  we observe between 80–100 m at  $8^\circ\text{N}$  during March and April (Table B1). Perhaps artificially high background mixing is partly to blame for the biases noted by Chowdary et al. (2016).

<sup>7</sup>for example, Jochum (2009), CCSM4 (Danabasoglu et al. 2012) and Chowdary et al. (2016).

### c. The importance of turbulence for salt flux at $8^\circ\text{N}$

Is the observed seasonally-enhanced mixing in the south-central Bay’s thermocline between May and November important for the Bay’s salt budget? The climatological depth of the  $S = 34.75$  psu surface at  $8^\circ\text{N}$  estimated using the Argo mapped climatology shallows by 20 m or so between May and November relative to other months (Figures C2k–o and C3f–i). The seasonal shallowing of this isohaline is significant since the observed diffusivity profile is surface intensified (Figure C7). Mean  $K_T$  at this isohaline, thick orange horizontal line in Figure C7, is approximately  $10^{-4} \text{ m}^2 \text{ s}^{-1}$  between May and November (SW; SWNE). In contrast,  $K_T$  is an order of magnitude lower during the NE monsoon and near-molecular during the NESW transition. Seasonally averaged surface velocities show the mean path of the SMC to be along the mooring line at  $8^\circ\text{N}$  (NRL3, NRL4, and NRL5; Figure C2a–e). So we now attempt to quantify turbulent salt flux along  $8^\circ\text{N}$  in the south-central Bay using our admittedly sparse dataset.

All available hourly averaged estimates of turbulent salt flux  $J_s^t$  are shown as a function of time in both depth and salinity spaces (Figure C10a,b respectively). Monthly averages of  $J_s^t$  in bins with edges defined by salinity surfaces  $S = [34, 34.5, 35, 36]$  psu (Figure C10c) are interpreted as the mean flux through the 34.25, 34.75, and 35.5 psu isohalines respectively. Bins with less than one instrument-month of data are not shown, those with less than two instrument months of data are grayed out and only one bin has more than three instrument-months of data (Figure C10c). Given the year-long coverage in the  $35 \leq S \leq 34.5$  salinity bin, we define the high salinity water mass as parcels with salinity  $S > 34.75$  psu (Figure C10b)<sup>8</sup>. An estimate of the virtual surface salinity flux  $S_0(E - P)$ , computed using evaporation  $E$  from OAFflux (Yu et al. 2008), precipitation  $P$  from the TRMM Multi-satellite Precipitation Analysis dataset (Huffman et al. 2007) and  $S_0 = 32$  psu, and averaged along  $8^\circ\text{N}$  between  $85^\circ\text{E}$  and  $90^\circ\text{E}$  is also presented for comparison (Figure C10d).

The  $\chi_{\text{pods}}$  recorded turbulent transport of salt through the  $S = 34.75$  psu isohaline between August and January<sup>9</sup> (Figure C10c). The timing of this turbulent salt flux in Figure C10d agrees with previous modelling studies that have highlighted the importance of vertical mixing during the SW monsoon and post-monsoon (SWNE) period in restoring the near-surface salinity of the Bay after the large freshwater input in August (Benshila et al. 2014; Akhil et al. 2014; Wilson and Riser 2016). The estimated mean value of  $J_s^t$  is of comparable magnitude to monthly

<sup>8</sup>Typically, investigators define this water mass to be  $S > 35$  psu (for e.g. Vinayachandran et al. 2013)

<sup>9</sup>Despite the absence of an organized SMC after September, relatively weakly-stratified high salinity water is still present in the south-central Bay (Figure C2o and low  $N^2$  in Figure C6d).

average surface virtual salinity flux  $S_0(E - P)$  averaged along  $8^\circ\text{N}$  between  $85^\circ\text{E}$  and  $90^\circ\text{E}$  (Figure C10d). For the upper 30m of the Bay, Wilson and Riser (2016) estimate that the freshwater input is primarily balanced by vertical advection and mixing that averages approximately  $2.5 \times 10^{-6}$  psu m/s upward between June and November — this may be interpreted as a flux at the base of the mixed layer. Our observations capture turbulent flux of that magnitude in September and October at depths of approximately 50–75 m (Figure C10a).

The sampling bias resulting from mooring blowdown suggests that we are underestimating the true magnitude of  $J_s^l$ . For example, all  $\chi$ pods at  $8^\circ\text{N}$  are forced down approximately 50 m or so by the Summer Monsoon Current in July during which time they record little turbulent salt flux (Figure C10a). Inspection of the velocity fields shows that the  $\chi$ pods dive beneath the region of greatest shear in the water column and are likely missing the regions of greatest mixing during this period (Figure C5). Given these uncertainties, we do not consider Figure C10c a good estimate of the amplitude of the seasonal cycle of turbulent heat flux but instead interpret it as evidence that climatologically important turbulent fluxes occur in the south-central Bay at least between August and January. Further extended observational efforts are required to properly constrain the magnitude of  $J_s^l$ .

## 5. Summary and future directions

Year-long observations of turbulence from moored mixing meters ( $\chi$ pods) revealed a seasonal cycle in upper-ocean turbulence along  $8^\circ\text{N}$  in the Bay of Bengal (Figures C3, C7 and Table C1). In the Bay's thermocline, the seasonal cycle of turbulence is influenced by downward propagating near-inertial waves and by low frequency shear associated with the Summer Monsoon Current and other mesoscale features such as the Sri Lanka Dome (Figures C6, C5 and C9). Multiple  $\chi$ pods recorded extended periods of weak mixing ( $1-10 \kappa_T$ ) between 50m and 100m depth during the months of March and April — a period of weak winds, weak currents, weak shear and low near-inertial energy input (Figures C2, C5 and C6; Tables B1,B2). It has been hypothesized that mixing in the vicinity of  $8^\circ\text{N}$  is necessary to close both heat and salt budgets in the Bay (Shenoi et al. 2002; Vinayachandran et al. 2013; Wilson and Riser 2016). Despite these extended periods of low mixing, our observations suggest that turbulent salt fluxes of the right magnitude are indeed occurring in the south-central Bay (Section 3c).

Fully interpreting the observed seasonal cycle of mixing requires understanding the processes that drive and sustain the Bay's internal wave field. The  $\chi$ pod observations show that enhanced thermocline mixing generally coincides with bursts of near-inertial shear. Understanding the

many mechanisms and processes that drive the seasonal cycle of near-inertial shear at depth is thus of prime importance. It is known that the stratified transition layer at the base of the mixed layer can strongly influence the ability of winds to drive energy into the thermocline. Dohan and Davis (2011) studied observations during two different storms. In one case they found that the wind-forced energy deepened the mixed layer with little to no mixing in the transition layer. For a second storm of comparable magnitude, the mixed layer remain unchanged but transition layer was significantly broadened through mixing in the thermocline. Brannigan et al. (2013) show that shear at the base of the transition layer depends on the alignment between ocean shear and wind stress. Both studies imply that the near-surface fresh water layer that characterizes the Bay could have a significant influence on the internal wave energy that ultimately leads to observed mixing. Lucas et al. (2016) found this to be the case in the Bay — they observed enhanced shear at the base of mixed layer but weak shear at the base of the barrier layer thereby isolating the thermocline from surface forcing. This picture may be complicated by other physics; for e.g. the interaction of near-inertial energy with lower-frequency mesoscale features in the Bay (Johnston et al. 2016). Another related puzzle is the extended period of weak to negligible mixing during March and April. This observation suggests that the Bay's internal wave field can be weaker than that expected from the Garrett-Munk spectrum typical of other oceanic regions, again highlighting the need for further study on the Bay's internal wave field. The Bay's complex upper ocean structure, seasonally varying winds, and strong synoptic storm activity offer intriguing opportunities for studying the ocean's internal wave field and its links to turbulence.

*Acknowledgments.* This work was supported by US Office of Naval Research grant numbers N00014-15-1-2634 and N00014-17-2472. Processed turbulence datasets and EBoB mooring data are available from the authors upon request. We thank two anonymous reviewers as well as the Editor for their fair and critical feedback. We also acknowledge expert engineering and technical contributions from Pavan Vutukur, Kerry Latham and Craig van Appledorn, and many stimulating discussions with Johannes Becherer, Alexis Kaminski, Sally Warner, Debasis Sengupta, J. Sree Lekha, Dipanjan Chaudhari, Eric D'Asaro and Jennifer MacKinnon. Many of these discussions were facilitated by a visit to the International Centre for Theoretical Sciences (ICTS) for participating in the program - Air-sea Interactions in the Bay of Bengal From Monsoons to Mixing (Code: ICTS/ommbob2019/02). The Ssalto/Duacs altimeter products were produced and distributed by the Copernicus Marine and Environment Monitoring Service (CMEMS) (<http://www.marine.copernicus.eu>). The OSCAR data were obtained from

JPL Physical Oceanography DAAC and developed by ESR (Earth and Space Research). The evaporation product was provided by the WHOI OAFflux project (<http://oaf Flux.who i .edu>) funded by the NOAA Climate Observations and Monitoring (COM) program. Analysis was greatly helped by the use of the xarray Python package (Hoyer and Hamman 2017). Development of xarray was partially supported by NSF Award 1740648 that funds the Pangeo platform.

## APPENDIX A

### Near-inertial input ( $\Pi_{\text{slab}}$ ) calculation

Near-inertial energy input  $\Pi_{\text{slab}}$  is calculated following Alford (2003)'s spectral solution of the Pollard and Millard (1970) slab ocean mixed layer model. In this model, mixed layer velocity  $Z = u + iv$  is obtained by solving

$$\frac{dZ}{dt} + (r + if)Z = \frac{T}{H} \quad (\text{A1})$$

where  $T = \rho_0^{-1}(\tau_x + i\tau_y)$ ,  $(\tau_x, \tau_y)$  is the wind stress,  $\rho_0$  is chosen to be  $1025 \text{ kg m}^{-3}$ ,  $H$  is the mixed layer depth,  $f$  is the Coriolis frequency and  $r$  is a damping coefficient that models the decay of mixed layer near-inertial energy. We follow Alford (2003) and choose  $r = 0.15f$ . Near-inertial energy input  $\Pi_{\text{slab}} = \Re[\rho Z T^*]$  is estimated by solving for  $Z$  in the frequency domain as in Alford (2003). This solution requires specification of wind stress  $T$  and mixed layer depth  $H$ . We choose to use hourly MERRA-2 reanalysis wind speeds (Modern-Era Retrospective Analysis for Research and Applications, Version 2; Gelaro et al. 2017) and monthly mean mixed layer depth from the monthly-mean MIMOC climatology (A Global Monthly Isopycnal Upper-Ocean Climatology with Mixed Layers; Schmidt et al. 2013). MIMOC's mixed layer depth estimates in the open ocean are primarily sourced from Argo profiles (Schmidt et al. 2013). There are flaws associated with this calculation (Plueddemann and Farrar 2006) but we believe Figure C2 captures the qualitative large-scale spatial and seasonal variation of the true near-inertial input  $\Pi$ . Another source of errors is that MERRA-2 does not capture the large wind stresses evident in the TropFlux compilation (Kumar et al. 2012) as well as in *in-situ* RAMA (The Research Moored Array for AfricanAsianAustralian Monsoon Analysis and Prediction) mooring sites in the Bay. However one cannot use Tropflux to calculate  $\Pi$  north of approximately  $10^\circ\text{N}$  because the inertial period nears 2 days, the Nyquist frequency of the daily resolution TropFlux winds.

## APPENDIX B

### Detecting weak turbulence

The voltage recorded by the FP-07 temperature sensor in the  $\chi$ pod is differentiated by an analog differentiator circuit and then digitized using an analog-to-digital converter (ADC) whose noise level is 6 voltage levels peak-to-peak. We estimate the spectral energy level of the discretized white noise voltage time series of that amplitude for a 1 second subset of data and combine it with the instrument calibration coefficients as in Becherer and Moum (2017) to get a dimensional spectral energy density level that would result when the ADC records "bit noise". Multiplying this noise spectral energy density level by frequency bandwidth gives an estimate of the instrument's "noise floor" i.e. an estimate of the variance in a one second interval when the data recorded is bit noise.

## APPENDIX C

### Tables of seasonal mean and seasonal median $K_T$

Tables B1 and B2 tabulate seasonal mean and seasonal median  $K_T$  along with 95% bootstrap confidence intervals.

## References

- Akhil, V. P., and Coauthors, 2014: A modeling study of the processes of surface salinity seasonal cycle in the Bay of Bengal. *J. Geophys. Res. Oceans*, **119** (6), 3926–3947, doi:10/gftfpw.
- Alford, M. H., 2001: Fine-Structure Contamination: Observations and a Model of a Simple Two-Wave Case. *J. Phys. Oceanogr.*, **31** (9), 2645–2649, doi:10.1175/1520-0485(2001)031<2645:FSCOA>2.0.CO;2.
- Alford, M. H., 2003: Improved global maps and 54-year history of wind-work on ocean inertial motions. *Geophys. Res. Lett.*, **30** (8), doi:10.1029/2002GL016614.
- Alford, M. H., and M. C. Gregg, 2001: Near-inertial mixing: Modulation of shear, strain and microstructure at low latitude. *J. Geophys. Res. Oceans*, **106** (C8), 16 947–16 968, doi:10.1029/2000JC000370.
- Alford, M. H., J. A. MacKinnon, R. Pinkel, and J. M. Klymak, 2017: SpaceTime Scales of Shear in the North Pacific. *J. Phys. Oceanogr.*, **47** (10), 2455–2478, doi:10.1175/JPO-D-17-0087.1.
- Batchelor, G. K., 1959: Small-scale variation of convected quantities like temperature in turbulent fluid Part 1. General discussion and the case of small conductivity. *J. Fluid Mech.*, **5** (01), 113, doi:10/fgvk78.
- Becherer, J., and J. N. Moum, 2017: An Efficient Scheme for Onboard Reduction of Moored pod Data. *J. Atmospheric Ocean. Technol.*, **34** (11), 2533–2546, doi:10.1175/JTECH-D-17-0118.1.
- Benshila, R., F. Durand, S. Masson, R. Bourdallé-Badie, C. de Boyer Montégut, F. Papa, and G. Madec, 2014: The upper Bay of Bengal salinity structure in a high-resolution model. *Ocean Model.*, **74**, 36–52, doi:10/f5rntg.
- Bonjean, F., and G. S. E. Lagerloef, 2002: Diagnostic Model and Analysis of the Surface Currents in the Tropical Pacific Ocean. *J. Phys. Oceanogr.*, **32** (10), 2938–2954, doi:10.1175/1520-0485(2002)032<2938:DMAAOT>2.0.CO;2.

- Brannigan, L., Y.-D. Lenn, T. P. Rippeth, E. McDonagh, T. K. Chereskin, and J. Sprintall, 2013: Shear at the Base of the Oceanic Mixed Layer Generated by Wind Shear Alignment. *J. Phys. Oceanogr.*, **43** (8), 1798–1810, doi:10.1175/JPO-D-12-0104.1.
- Chatterjee, A., and Coauthors, 2012: A new atlas of temperature and salinity for the North Indian Ocean. *J. Earth Syst. Sci.*, **121** (3), 559–593, doi:10.1007/s12040-012-0191-9.
- Chen, G., Y. Li, Q. Xie, and D. Wang, 2018: Origins of Eddy Kinetic Energy in the Bay of Bengal. *J. Geophys. Res. Oceans*, doi:10.1002/2017JC013455.
- Chowdary, J. S., A. Parekh, G. Srinivas, C. Gnanaseelan, T. Fousiya, R. Khandekar, and M. K. Roxy, 2016: Processes Associated with the Tropical Indian Ocean Subsurface Temperature Bias in a Coupled Model. *J. Phys. Oceanogr.*, **46** (9), 2863–2875, doi:10.1175/JPO-D-15-0245.1.
- Danabasoglu, G., S. C. Bates, B. P. Briegleb, S. R. Jayne, M. Jochum, W. G. Large, S. Peacock, and S. G. Yeager, 2012: The CCSM4 Ocean Component. *J. Clim.*, **25** (5), 1361–1389, doi:10.1175/JCLI-D-11-00091.1.
- Dohan, K., and R. E. Davis, 2011: Mixing in the Transition Layer during Two Storm Events. *J. Phys. Oceanogr.*, **41** (1), 42–66, doi:10.1175/2010JPO4253.1.
- Durand, F., D. Shankar, F. Birol, and S. S. C. Shenoi, 2009: Spatiotemporal structure of the East India Coastal Current from satellite altimetry. *J. Geophys. Res.*, **114** (C2), doi:10.1029/2008JC004807.
- ESR, 2009: OSCAR third degree resolution ocean surface currents. NASA Physical Oceanography DAAC, doi:10.5067/OSCAR-03D01.
- Gadgil, S., 2003: The Indian Monsoon and its Variability. *Annu. Rev. Earth Planet. Sci.*, **31** (1), 429–467, doi:10.1146/annurev.earth.31.100901.141251.
- Gadgil, S., and K. Rupa Kumar, 2006: The Asian monsoon agriculture and economy. *The Asian Monsoon*, Springer Berlin Heidelberg, 651–683, doi:10.1007/3-540-37722-0\_18.
- Gargett, A. E., T. R. Osborn, and P. W. Nasmyth, 1984: Local isotropy and the decay of turbulence in a stratified fluid. *J. Fluid Mech.*, **144**, 231, doi:10/cvc896.
- Gelaro, R., and Coauthors, 2017: The Modern-Era Retrospective Analysis for Research and Applications, Version 2 (MERRA-2). *J. Clim.*, **30** (14), 5419–5454, doi:10.1175/JCLI-D-16-0758.1.
- Gordon, A., E. Shroyer, A. Mahadevan, D. Sengupta, and M. Freilich, 2016: Bay of Bengal: 2013 Northeast Monsoon Upper-Ocean Circulation. *Oceanography*, **29** (2), 82–91, doi:10.5670/oceanog.2016.41.
- Goswami, B. N., R. S. Ajayamohan, P. K. Xavier, and D. Sengupta, 2003: Clustering of synoptic activity by Indian summer monsoon intraseasonal oscillations. *Geophys. Res. Lett.*, **30** (8), doi:10/cjk2nw.
- Gregg, M., M. Alford, H. Kontoyiannis, V. Zervakis, and D. Winkel, 2012: Mixing over the steep side of the Cycladic Plateau in the Aegean Sea. *J. Mar. Syst.*, **89** (1), 30–47, doi:10/chjrbk.
- Gregg, M., E. D’Asaro, J. Riley, and E. Kunze, 2018: Mixing Efficiency in the Ocean. *Annu. Rev. Mar. Sci.*, **10** (1), doi:10.1146/annurev-marine-121916-063643.
- Gregg, M. C., T. B. Sanford, and D. P. Winkel, 2003: Reduced mixing from the breaking of internal waves in equatorial waters. *Nature*, **422** (6931), 513–515, doi:10.1038/nature01507.
- Henye, F. S., J. Wright, and S. M. Flatté, 1986: Energy and action flow through the internal wave field: An eikonal approach. *J. Geophys. Res. Oceans*, **91** (C7), 8487–8495, doi:10.1029/JC091iC07p08487.
- Hoyer, S., and J. J. Hamman, 2017: Xarray: N-D labeled Arrays and Datasets in Python. *J. Open Res. Softw.*, **5**, doi:10.5334/jors.148.
- Huffman, G. J., and Coauthors, 2007: The TRMM Multisatellite Precipitation Analysis (TMPA): Quasi-Global, Multiyear, Combined-Sensor Precipitation Estimates at Fine Scales. *J. Hydrometeorol.*, **8** (1), 38–55, doi:10/bkgg5q.
- Itsweire, E. C., J. R. Koseff, D. A. Briggs, and J. H. Ferziger, 1993: Turbulence in Stratified Shear Flows: Implications for Interpreting Shear-induced Mixing in the Ocean. *J. Phys. Oceanogr.*, **23** (7), 1508–1522, doi:10/cfdncr.
- Ivey, G., K. Winters, and J. Koseff, 2008: Density Stratification, Turbulence, but How Much Mixing? *Annu. Rev. Fluid Mech.*, **40** (1), 169–184, doi:10.1146/annurev.fluid.39.050905.110314.
- Jensen, T., H. Wijesekera, E. Nyadjro, P. Thoppil, J. Shriver, K. Sandeep, and V. Pant, 2016: Modeling Salinity Exchanges Between the Equatorial Indian Ocean and the Bay of Bengal. *Oceanography*, **29** (2), 92–101, doi:10/f8w92v.
- Jensen, T. G., 2001: Arabian Sea and Bay of Bengal exchange of salt and tracers in an ocean model. *Geophys. Res. Lett.*, **28** (20), 3967–3970, doi:10.1029/2001GL013422.
- Jinadasa, S., I. Lozovatsky, J. Planella-Morató, J. Nash, J. MacKinnon, A. Lucas, H. Wijesekera, and H. Fernando, 2016: Ocean Turbulence and Mixing Around Sri Lanka and in Adjacent Waters of the Northern Bay of Bengal. *Oceanography*, **29** (2), 170–179, doi:10.5670/oceanog.2016.49.
- Jochum, M., 2009: Impact of latitudinal variations in vertical diffusivity on climate simulations. *J. Geophys. Res.*, **114** (C1), doi:10.1029/2008JC005030.
- Johnston, S., D. Chaudhuri, M. Mathur, D. Rudnick, D. Sengupta, H. Simmons, A. Tandon, and R. Venkatesan, 2016: Decay Mechanisms of Near-Inertial Mixed Layer Oscillations in the Bay of Bengal. *Oceanography*, **29** (2), 180–191, doi:10.5670/oceanog.2016.50.
- Koul, V., A. Parekh, G. Srinivas, R. Kakatkar, J. S. Chowdary, and C. Gnanaseelan, 2018: Role of Ocean Initial Conditions to Diminish Dry Bias in the Seasonal Prediction of Indian Summer Monsoon Rainfall: A Case Study Using Climate Forecast System. *J. Adv. Model. Earth Syst.*, **10** (3), 603–616, doi:10.1002/2017MS001129.
- Kraichnan, R. H., 1968: Small-Scale Structure of a Scalar Field Convected by Turbulence. *Phys. Fluids*, **11** (5), 945, doi:10.1063/1.1692063.
- Kumar, B. P., J. Vialard, M. Lengaigne, V. S. N. Murty, and M. J. McPhaden, 2012: TropFlux: Air-sea fluxes for the global tropical oceansdescription and evaluation. *Clim. Dyn.*, **38** (7–8), 1521–1543, doi:10.1007/s00382-011-1115-0.
- Kunze, E., E. Firing, J. M. Hummon, T. K. Chereskin, and A. M. Thurnherr, 2006: Global Abyssal Mixing Inferred from Lowered ADCP Shear and CTD Strain Profiles. *J. Phys. Oceanogr.*, **36** (8), 1553–1576, doi:10.1175/JPO2926.1.

- Lucas, A., and Coauthors, 2016: Adrift Upon a Salinity-Stratified Sea: A View of Upper-Ocean Processes in the Bay of Bengal During the Southwest Monsoon. *Oceanography*, **29** (2), 134–145, doi:10.5670/oceanog.2016.46.
- Lueck, R. G., O. Hertzman, and T. R. Osborn, 1977: The spectral response of thermistors. *Deep Sea Res.*, **24** (10), 951–970, doi:10/cxnd39.
- Moum, J. N., 2015: Ocean Speed and Turbulence Measurements Using Pitot-Static Tubes on Moorings. *J. Atmospheric Ocean. Technol.*, **32** (7), 1400–1413, doi:10.1175/JTECH-D-14-00158.1.
- Moum, J. N., and J. D. Nash, 2009: Mixing Measurements on an Equatorial Ocean Mooring. *J. Atmospheric Ocean. Technol.*, **26** (2), 317–336, doi:10.1175/2008JTECHO617.1.
- Murty, V. S. N., Y. V. B. Sarma, D. P. Rao, and C. S. Murty, 1992: Water characteristics, mixing and circulation in the Bay of Bengal during southwest monsoon. *J. Mar. Res.*, **50** (2), 207–228, doi:10.1357/002224092784797700.
- Osborn, T. R., 1980: Estimates of the Local Rate of Vertical Diffusion from Dissipation Measurements. *J. Phys. Oceanogr.*, **10** (1), 83–89, doi:10.1175/1520-0485(1980)010<0083:EOTLRO>2.0.CO;2.
- Osborn, T. R., and C. S. Cox, 1972: Oceanic fine structure. *Geophys. Fluid Dyn.*, **3** (1), 321–345, doi:10.1080/03091927208236085.
- Perlin, A., and J. N. Moum, 2012: Comparison of Thermal Variance Dissipation Rates from Moored and Profiling Instruments at the Equator. *J. Atmospheric Ocean. Technol.*, **29** (9), 1347–1362, doi:10.1175/JTECH-D-12-00019.1.
- Pinkel, R., M. A. Goldin, J. A. Smith, O. M. Sun, A. A. Aja, M. N. Bui, and T. Hughen, 2011: The Wirewalker: A Vertically Profiling Instrument Carrier Powered by Ocean Waves. *J. Atmospheric Ocean. Technol.*, **28** (3), 426–435, doi:10.1175/2010JTECHO805.1.
- Plueddemann, A., and J. Farrar, 2006: Observations and models of the energy flux from the wind to mixed-layer inertial currents. *Deep Sea Res. Part II Top. Stud. Oceanogr.*, **53** (1–2), 5–30, doi:10.1016/j.dsr2.2005.10.017.
- Pollard, R., and R. Millard, 1970: Comparison between observed and simulated wind-generated inertial oscillations. *Deep Sea Res. Oceanogr. Abstr.*, **17** (4), 813–821, doi:10.1016/0011-7471(70)90043-4.
- Pujiana, K., J. N. Moum, and W. D. Smyth, 2018: The Role of Turbulence in Redistributing Upper-Ocean Heat, Freshwater, and Momentum in Response to the MJO in the Equatorial Indian Ocean. *J. Phys. Oceanogr.*, **48** (1), 197–220, doi:10.1175/JPO-D-17-0146.1.
- Roemmich, D., and J. Gilson, 2009: The 2004–2008 mean and annual cycle of temperature, salinity, and steric height in the global ocean from the Argo Program. *Prog. Oceanogr.*, **82** (2), 81–100, doi:10.1016/j.pocean.2009.03.004.
- Rohr, J. J., E. C. Itsweire, K. N. Helland, and C. W. V. Atta, 1988: Growth and decay of turbulence in a stably stratified shear flow. *J. Fluid Mech.*, **195**, 77, doi:10/cgxzqw.
- Roxy, M., 2014: Sensitivity of precipitation to sea surface temperature over the tropical summer monsoon region and its quantification. *Clim. Dyn.*, **43** (5–6), 1159–1169, doi:10.1007/s00382-013-1881-y.
- SanchezFranks, A., B. G. M. Webber, B. A. King, P. N. Vinayachandran, A. J. Matthews, P. M. F. Sheehan, A. Behara, and C. P. Neema, 2019: The Railroad Switch Effect of Seasonally Reversing Currents on the Bay of Bengal High Salinity Core. *Geophys. Res. Lett.*, doi:10/gf32bm.
- Scheifele, B., S. Waterman, L. Merckelbach, and J. R. Carpenter, 2018: Measuring the Dissipation Rate of Turbulent Kinetic Energy in Strongly Stratified, Low-Energy Environments: A Case Study From the Arctic Ocean. *J. Geophys. Res. Oceans*, **123** (8), 5459–5480, doi:10.1029/2017JC013731.
- Schmidtko, S., G. C. Johnson, and J. M. Lyman, 2013: MIMOC: A global monthly isopycnal upper-ocean climatology with mixed layers: MIMOC. *J. Geophys. Res. Oceans*, **118** (4), 1658–1672, doi:10.1002/jgrc.20122.
- Schott, F. A., M. Dengler, and R. Schoenefeldt, 2002: The shallow overturning circulation of the Indian Ocean. *Prog. Oceanogr.*, **53** (1), 57–103, doi:10.1016/S0079-6611(02)00039-3.
- Schott, F. A., and J. P. McCreary, 2001: The monsoon circulation of the Indian Ocean. *Prog. Oceanogr.*, **51** (1), 1–123.
- Sengupta, D., G. N. Bharath Raj, and S. S. C. Sheno, 2006: Surface freshwater from Bay of Bengal runoff and Indonesian Throughflow in the tropical Indian Ocean. *Geophys. Res. Lett.*, **33** (22), doi:10/bb5rwc.
- Shankar, D., P. N. Vinayachandran, and A. S. Unnikrishnan, 2002: The monsoon currents in the north Indian Ocean. *Prog. Oceanogr.*, **52** (1), 63–120.
- Sheno, S. S. C., D. Shankar, and S. R. Shetye, 2002: Differences in heat budgets of the near-surface Arabian Sea and Bay of Bengal: Implications for the summer monsoon. *J. Geophys. Res.*, **107** (C6), doi:10.1029/2000JC000679.
- St. Laurent, L., and S. Merrifield, 2017: Measurements of Near-Surface Turbulence and Mixing from Autonomous Ocean Gliders. *Oceanography*, **30** (2), 116–125, doi:10.5670/oceanog.2017.231.
- Vecchi, G. A., and D. E. Harrison, 2002: Monsoon Breaks and Sub-seasonal Sea Surface Temperature Variability in the Bay of Bengal. *J. Clim.*, **15** (12), 1485–1493, doi:10.1175/1520-0442(2002)015<1485:MBASS>2.0.CO;2.
- Vinayachandran, P. N., Y. Masumoto, T. Mikawa, and T. Yamagata, 1999: Intrusion of the southwest monsoon current into the Bay of Bengal. *J. Geophys. Res. Oceans*, **104** (C5), 11 077–11 085.
- Vinayachandran, P. N., D. Shankar, S. Vernekar, K. K. Sandeep, P. Amol, C. P. Neema, and A. Chatterjee, 2013: A summer monsoon pump to keep the Bay of Bengal salty. *Geophys. Res. Lett.*, **40** (9), 1777–1782, doi:10.1002/grl.50274.
- Vinayachandran, P. N., and T. Yamagata, 1998: Monsoon Response of the Sea around Sri Lanka: Generation of Thermal Domes and Anticyclonic Vortices. *J. Phys. Oceanogr.*, **28** (10), 1946–1960, doi:10.1175/1520-0485(1998)028<1946:MRO TSA>2.0.CO;2.
- Webber, B. G. M., A. J. Matthews, P. N. Vinayachandran, C. P. Neema, A. Sanchez-Franks, V. Vijith, P. Amol, and D. B. Baranowski, 2018: The dynamics of the Southwest Monsoon current in 2016 from high-resolution in situ observations and models. *J. Phys. Oceanogr.*, **48** (10), 2259–2282, doi:10.1175/JPO-D-17-0215.1.
- Wijesekera, H. W., W. J. Teague, D. W. Wang, E. Jarosz, T. G. Jensen, S. U. P. Jinadasa, H. J. S. Fernando, and Z. R. Hallock,

- 2016: Low-Frequency Currents from Deep Moorings in the Southern Bay of Bengal. *J. Phys. Oceanogr.*, **46** (10), 3209–3238, doi:10.1175/JPO-D-16-0113.1.
- Wijesekera, H. W., and Coauthors, 2015: Southern Bay of Bengal currents and salinity intrusions during the northeast monsoon. *J. Geophys. Res. Oceans*, **120** (10), 6897–6913, doi:10.1002/2015JC010744.
- Wilson, E. A., and S. C. Riser, 2016: An Assessment of the Seasonal Salinity Budget for the Upper Bay of Bengal. *J. Phys. Oceanogr.*, **46** (5), 1361–1376, doi:10/f8ms36.
- Yu, L., X. Jin, and R. A. Weller, 2008: Multidecade Global Flux Datasets from the Objectively Analyzed Air-sea Fluxes (OAFlux) Project: Latent and Sensible Heat Fluxes, Ocean Evaporation, and Related Surface Meteorological Variables. 64.

Table C1. Bay of Bengal  $\chi$ pod deployments described in this paper.

	Location	Depth [m]	Duration of valid data return
NRL3	85.5E, 8N	32 (28-78)	20 Dec 2013 - 12 Dec 2014
		52 (48-100)	28 Dec 2014
NRL4	87E, 8N	63 (60-85)	21 Dec 2013 - 28 Dec 2014
		83 (80-105)	09 Feb 2015
NRL5	88.5E, 8N	85	21 Dec 2013 - 30 Jan 2015
		105	22 Feb 2015

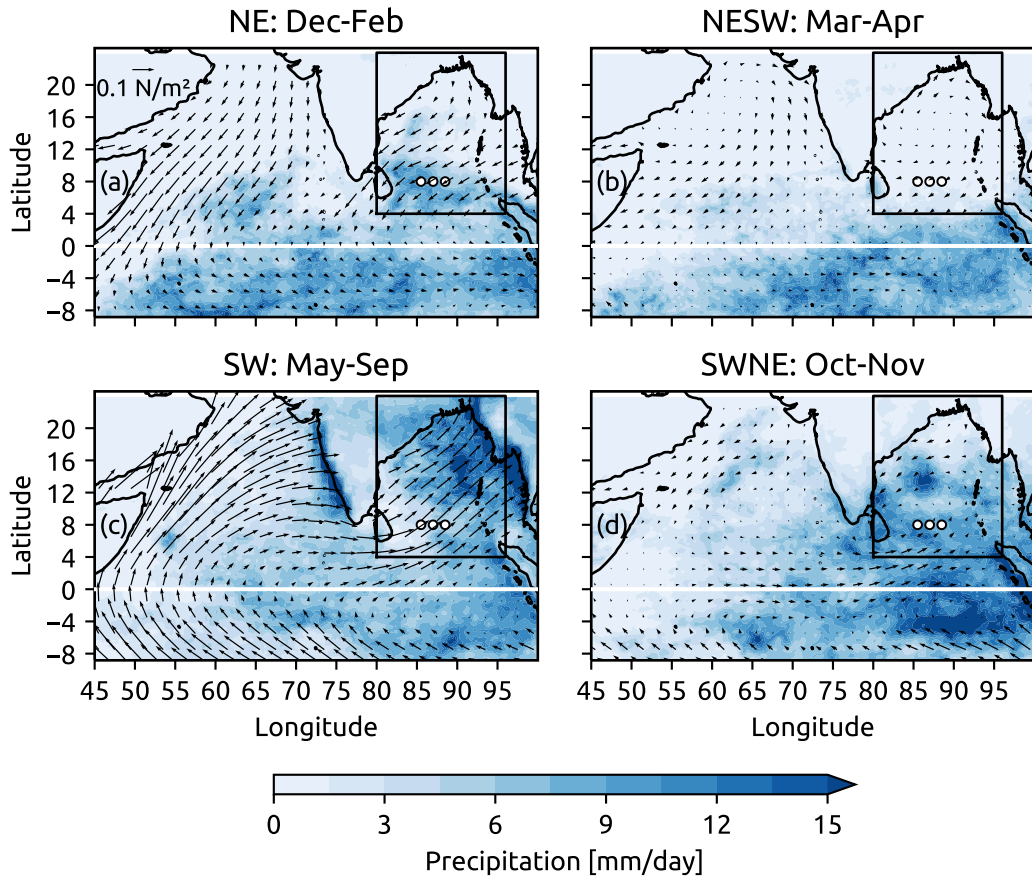


Figure C1. Seasonal mean wind stress over the ocean from Tropflux (arrows; Kumar et al. 2012) and precipitation from the TRMM Multi-satellite Precipitation Analysis dataset (color; Huffman et al. 2007) over the Indian Ocean basin north of 10°S averaged between December, 2013 and November, 2014. Black box marks Bay of Bengal region shown in Figure C2. White dots mark mooring locations.

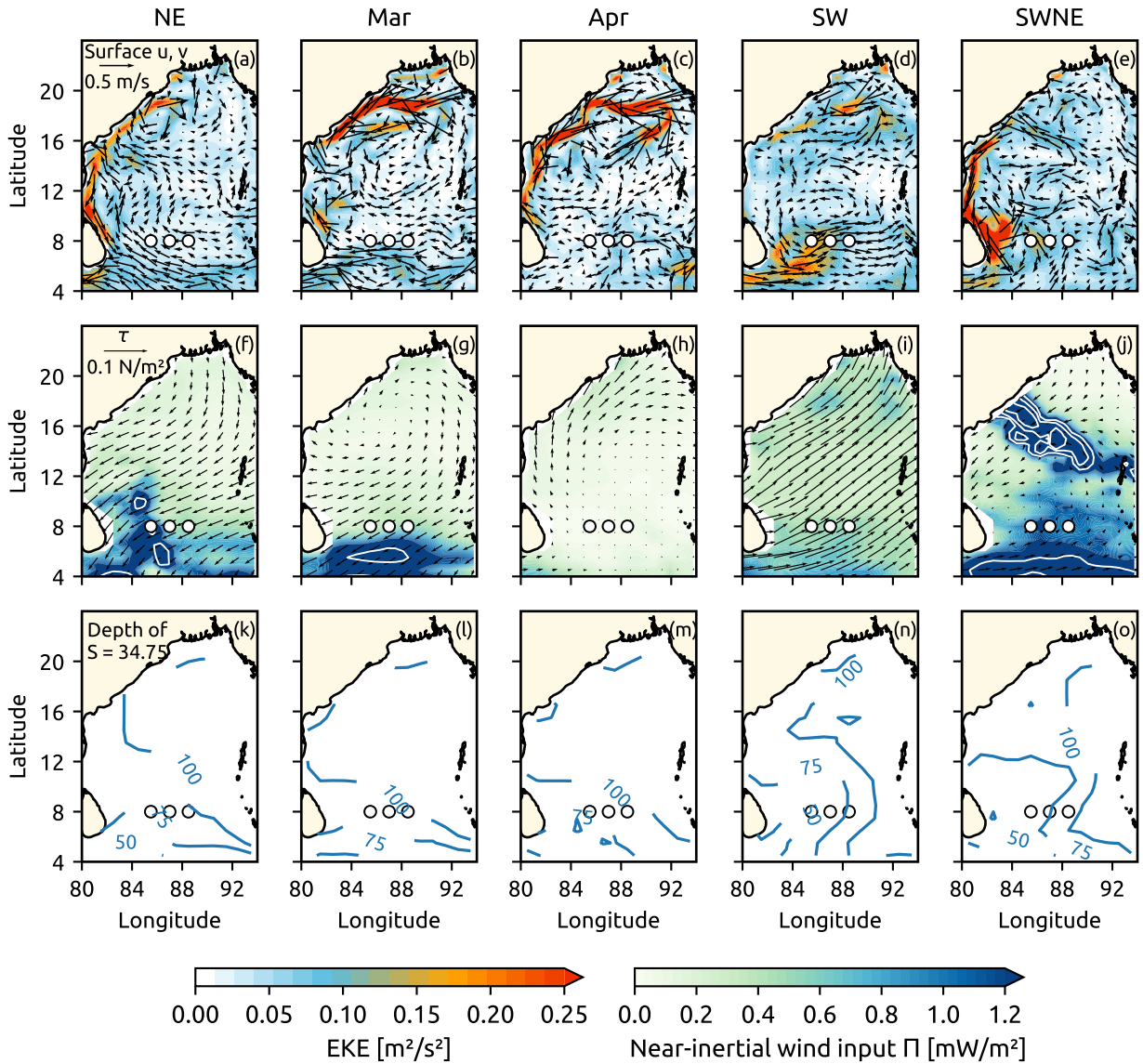


Figure C2. Seasonal cycle of forcing and circulation in the Bay of Bengal for 2014. White dots mark mooring locations used in the study. (top) Seasonal mean geostrophic eddy kinetic energy (EKE) from altimeter sea surface height (SSH) in color; vectors indicate surface currents from seasonally averaged 5-day OSCAR estimate (ESR 2009; Bonjean and Lagerloef 2002). (middle) Seasonal near-inertial energy input calculated using a slab ocean mixed layer model  $\Pi_{\text{slab}}$  (Appendix A). White contours are  $\Pi = 2, 4$  and  $10 \text{ mW m}^{-2}$ . (bottom) 50, 75 and 100-m depth contours of the 34.75 isohaline surface from the Argo mapped climatology of subsurface temperature and salinity (Roemmich and Gilson 2009). Similar results were obtained using the North Indian Ocean Atlas of Chatterjee et al. (2012). The months of March and April are separated to emphasize the basin-wide weak mean wind stress and weak near-inertial input.

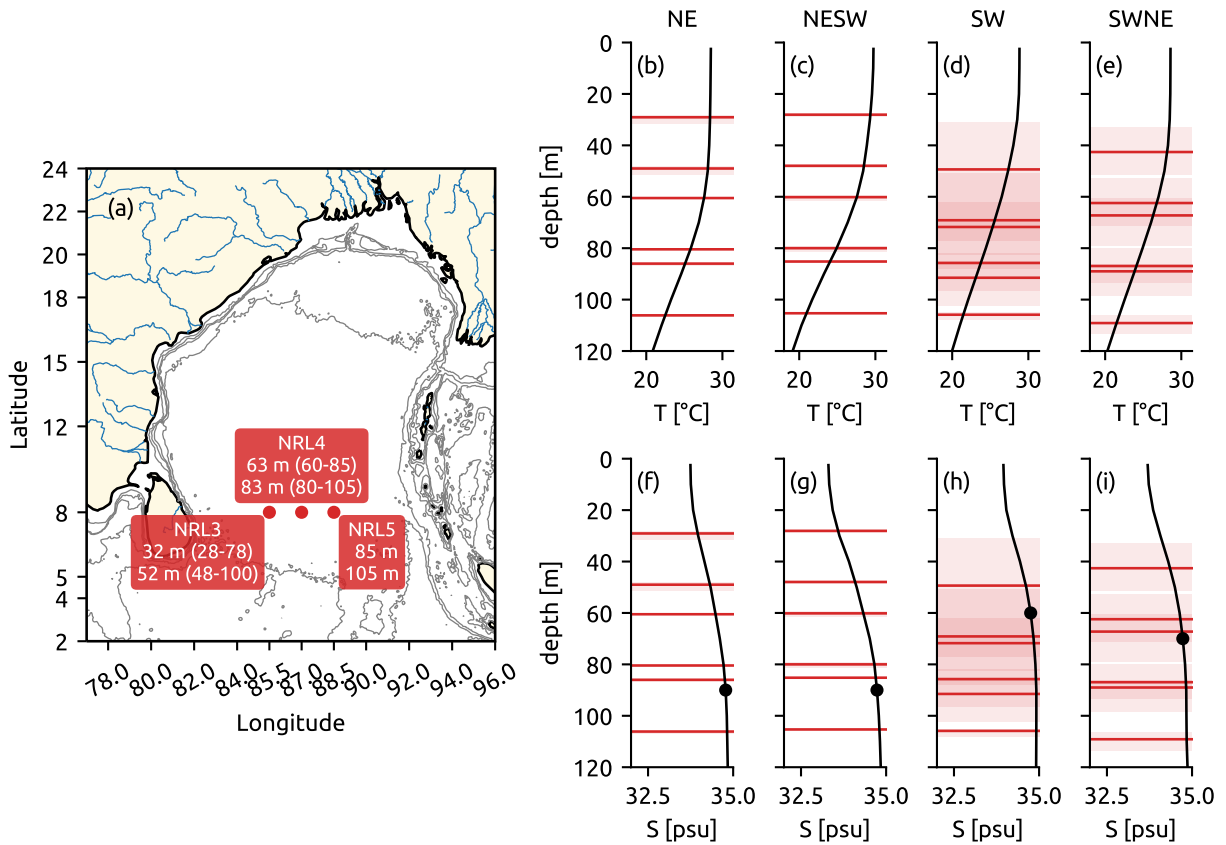


Figure C3. 2014  $\chi$ pod deployment at  $8^{\circ}\text{N}$ . (a) Locations of moorings. (b–i) Seasonal mean temperature (b–e) and salinity (f–i) profiles from the Argo climatology, averaged along  $8^{\circ}\text{N}$  between  $85.5^{\circ}\text{E}$  and  $88.5^{\circ}\text{E}$ . These moorings experienced significant blowdown during the SW monsoon and the postmonsoon SWNE period. Horizontal lines and shading mark median and interquartile range of each  $\chi$ pod's depth for these two seasons. The black dot marks  $S = 34.75$  psu. Temperature and salinity axes (lower and upper x-axes) are scaled such that axis limits represent equal jumps in density so panels (b–i) indicate that the mean stratification at the  $\chi$ pod depth levels is dominated by temperature in the long-term mean.

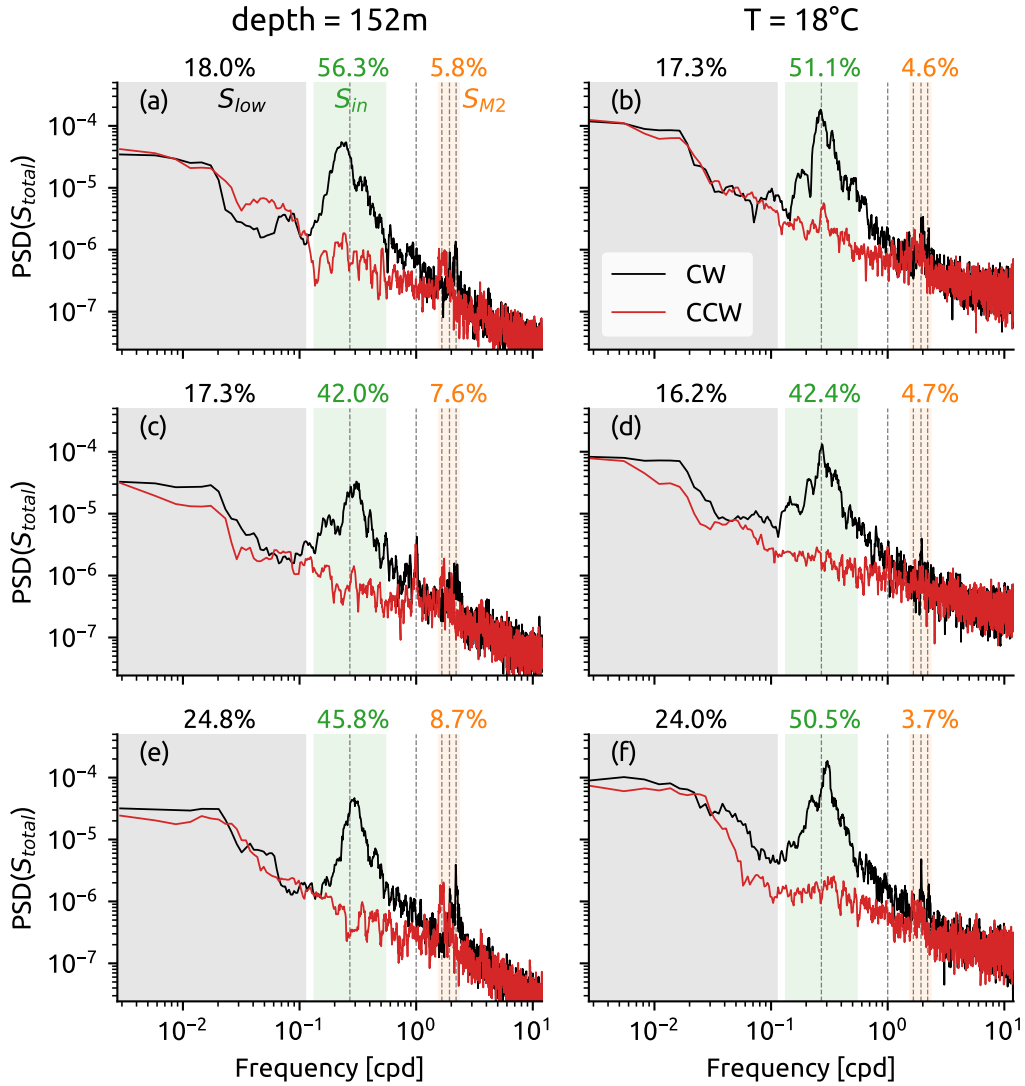


Figure C4. Rotary power spectral density of total shear  $S_{total}$  at all three moorings estimated using the multitaper method. (a, c, e) Eulerian estimate at 152 m; (b, d, f) isothermal estimate at the 18°C isotherm. Lowpass, near-inertial and near-tidal bands (colored shading: gray, green, orange respectively) as well as percentage of total shear variance in each band (colored text) are shown. Vertical lines mark  $f_0$ , the diurnal frequency,  $\omega_{M2} - f_0$  and  $\omega_{M2} + f_0$ . Clockwise and counter-clockwise spectra are in black and red respectively.

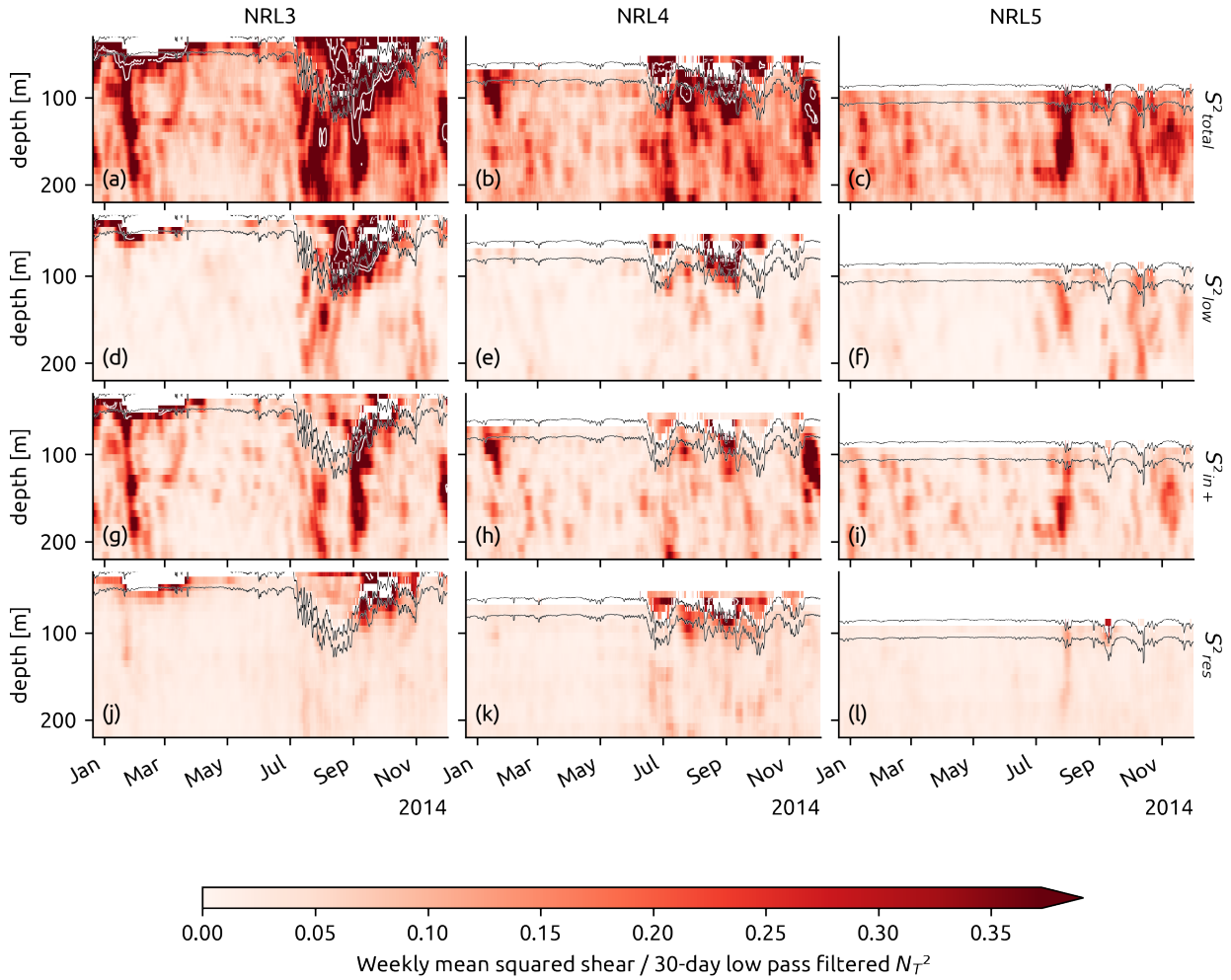


Figure C5. Weekly running mean-squared shear for the three moorings (top to bottom): (a-c) total shear  $S^2_{total}$ ; (d-f) low-frequency shear  $S^2_{low}$ ; (g-i) total near-inertial shear  $S^2_{in+}$ ; (j-l) residual shear  $S^2_{res}$ . All components are normalized by the normalized by 30-day lowpass filtered  $N_T^2 = g\alpha T_z$ . Regions with  $N_T^2 < 10^{-5} \text{ s}^{-2}$  are excluded.  $\chi$ pod depths for both  $\chi$ -pods are shown in black in all panels. White contours mark levels 0.75, 1.25.

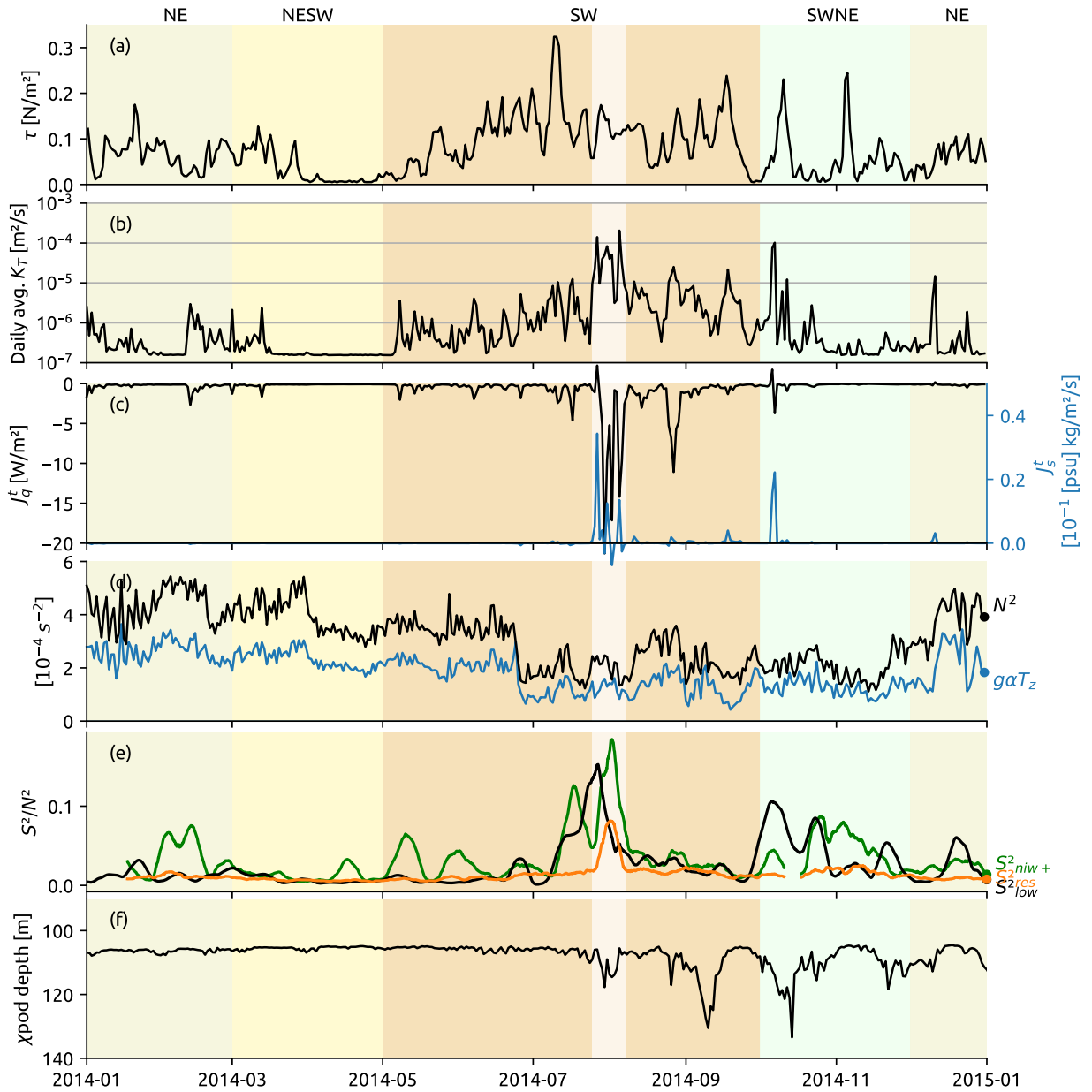


Figure C6. A year of observations at NRL5, 105m. Time series of daily averaged quantities: (a) Tropflux wind stress; (b) daily averaged  $K_T$ ; (c) turbulent heat and salt fluxes  $J_q^t, J_s^t$ ; (d) Buoyancy frequency  $N^2$  and temperature contribution to  $N^2$ ,  $N_T^2 = g\alpha T_z$ ; (e) Weekly running mean of filtered squared shear magnitude normalized by  $N^2$ : low pass in black  $S_{low}^2$ , near-inertial bandpass  $S_{in+}^2$  in green and the residual  $S_{res}^2$  in orange; (f)  $\chi$ pod depth. Background colors mark seasons; white region indicates time period shown in Figure C9.

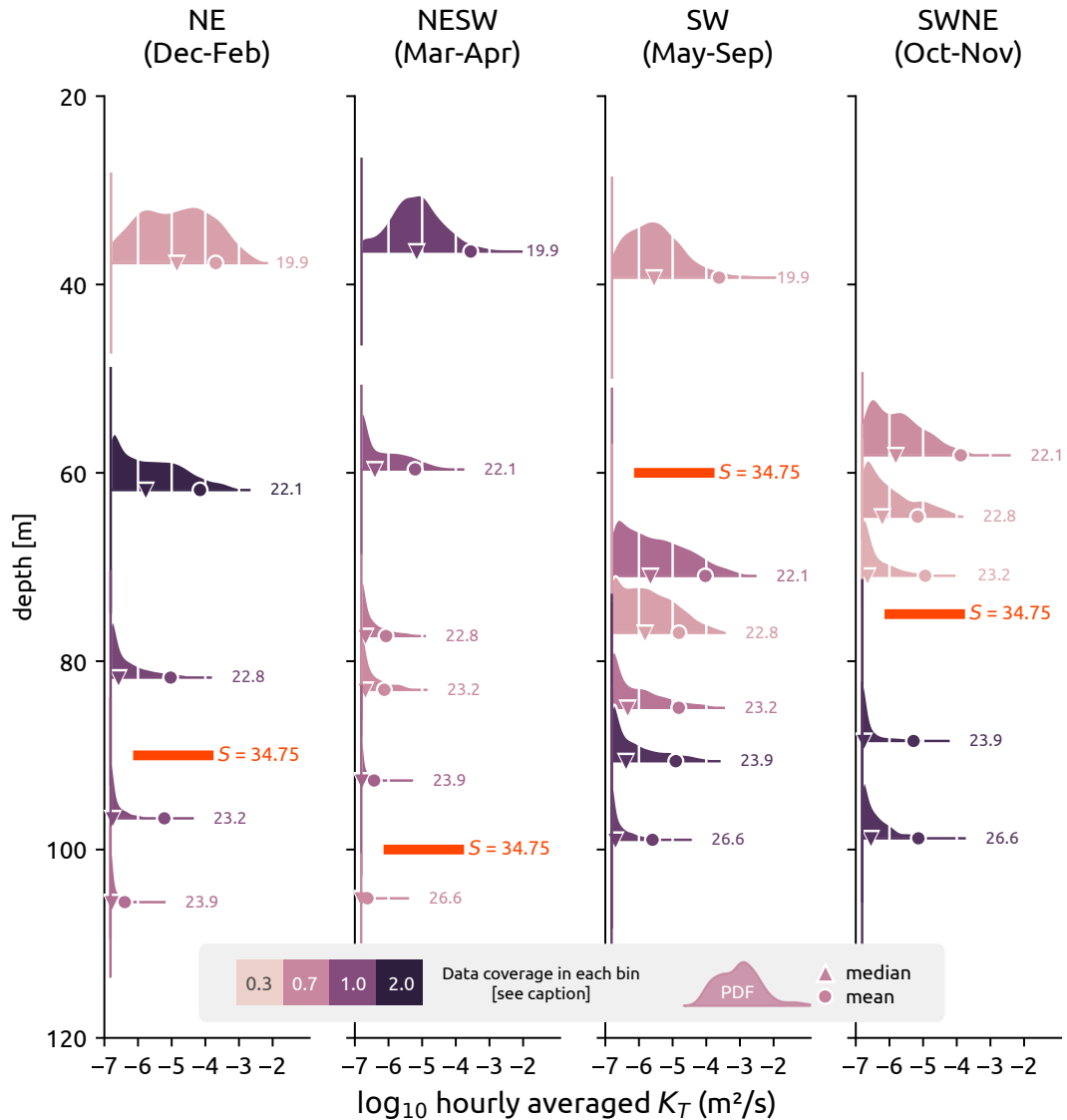


Figure C7. The seasonal cycle of  $K_T$  at  $8^\circ\text{N}$ . Vertical profile of hourly averaged  $K_T$  formed by combining all estimates in density bins (Section c). PDFs as well as means and medians are shown. Bins are marked by  $\rho - 1000$ . Orange horizontal lines mark the climatological depth of the  $S = 34.75$  isohaline at  $8^\circ\text{N}$  estimated using the Argo climatology. Vertical lines mark the standard deviation of measurement depths in each bin — these lines tend to overlap each other. Each PDF is colored according to data coverage: one means that there is at least one hourly estimate for every hour in the season.

Table C2. Table of mean  $K_T$  ( $10^{-6} \text{ m}^2 \text{ s}^{-1}$ ) and bootstrap 95% confidence intervals.

season bin	NE	NESW	SW	SWNE
(1018.0, 1021.7]	203.98 <sup>282.16</sup> <sub>158.37</sub>	276.92 <sup>455.38</sup> <sub>181.38</sub>	240.55 <sup>440.42</sup> <sub>156.69</sub>	53.79 <sup>82.21</sup> <sub>36.57</sub>
(1021.7, 1022.5]	69.73 <sup>93.30</sup> <sub>54.64</sub>	6.16 <sup>8.42</sup> <sub>4.86</sub>	94.09 <sup>179.59</sup> <sub>69.29</sub>	131.34 <sup>333.04</sup> <sub>33.92</sub>
(1022.5, 1023.0]	9.30 <sup>27.00</sup> <sub>4.88</sub>	0.84 <sup>1.10</sup> <sub>0.73</sub>	15.39 <sup>19.23</sup> <sub>12.88</sub>	6.91 <sup>9.11</sup> <sub>5.48</sub>
(1023.0, 1023.5]	6.06 <sup>16.97</sup> <sub>1.95</sub>	0.75 <sup>0.91</sup> <sub>0.65</sub>	15.23 <sup>28.04</sup> <sub>10.50</sub>	11.53 <sup>55.27</sup> <sub>2.44</sub>

Table C3. Table of median  $K_T$  ( $10^{-6} \text{ m}^2 \text{ s}^{-1}$ ) and bootstrap 95% confidence intervals.

season bin	median $K_T$			
	NE	NESW	SW	SWNE
(1018.0, 1021.7]	14.32 <sup>18.38</sup> <sub>11.41</sub>	6.89 <sup>7.55</sup> <sub>6.29</sub>	2.81 <sup>3.19</sup> <sub>2.44</sub>	11.35 <sup>13.52</sup> <sub>8.44</sub>
(1021.7, 1022.5]	1.70 <sup>1.91</sup> <sub>1.48</sub>	0.40 <sup>0.46</sup> <sub>0.34</sub>	2.19 <sup>2.45</sup> <sub>1.93</sub>	1.55 <sup>1.80</sup> <sub>1.25</sub>
(1022.5, 1023.0]	0.26 <sup>0.28</sup> <sub>0.25</sub>	0.21 <sup>0.22</sup> <sub>0.19</sub>	1.52 <sup>1.68</sup> <sub>1.31</sub>	0.62 <sup>0.72</sup> <sub>0.52</sub>
(1023.0, 1023.5]	0.18 <sup>0.18</sup> <sub>0.17</sub>	0.21 <sup>0.22</sup> <sub>0.20</sub>	0.46 <sup>0.52</sup> <sub>0.42</sub>	0.22 <sup>0.25</sup> <sub>0.20</sub>

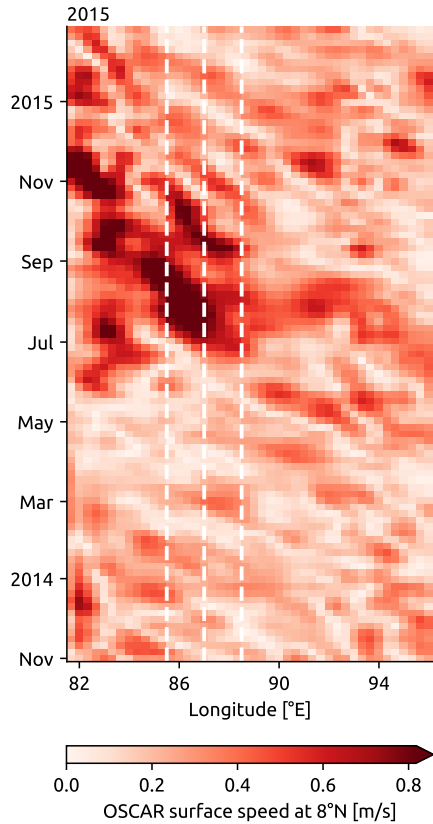


Figure C8. Hovmoeller diagram of near-surface speed at 8°N as estimated in the OSCAR product. Vertical white dashed lines indicate mooring locations.

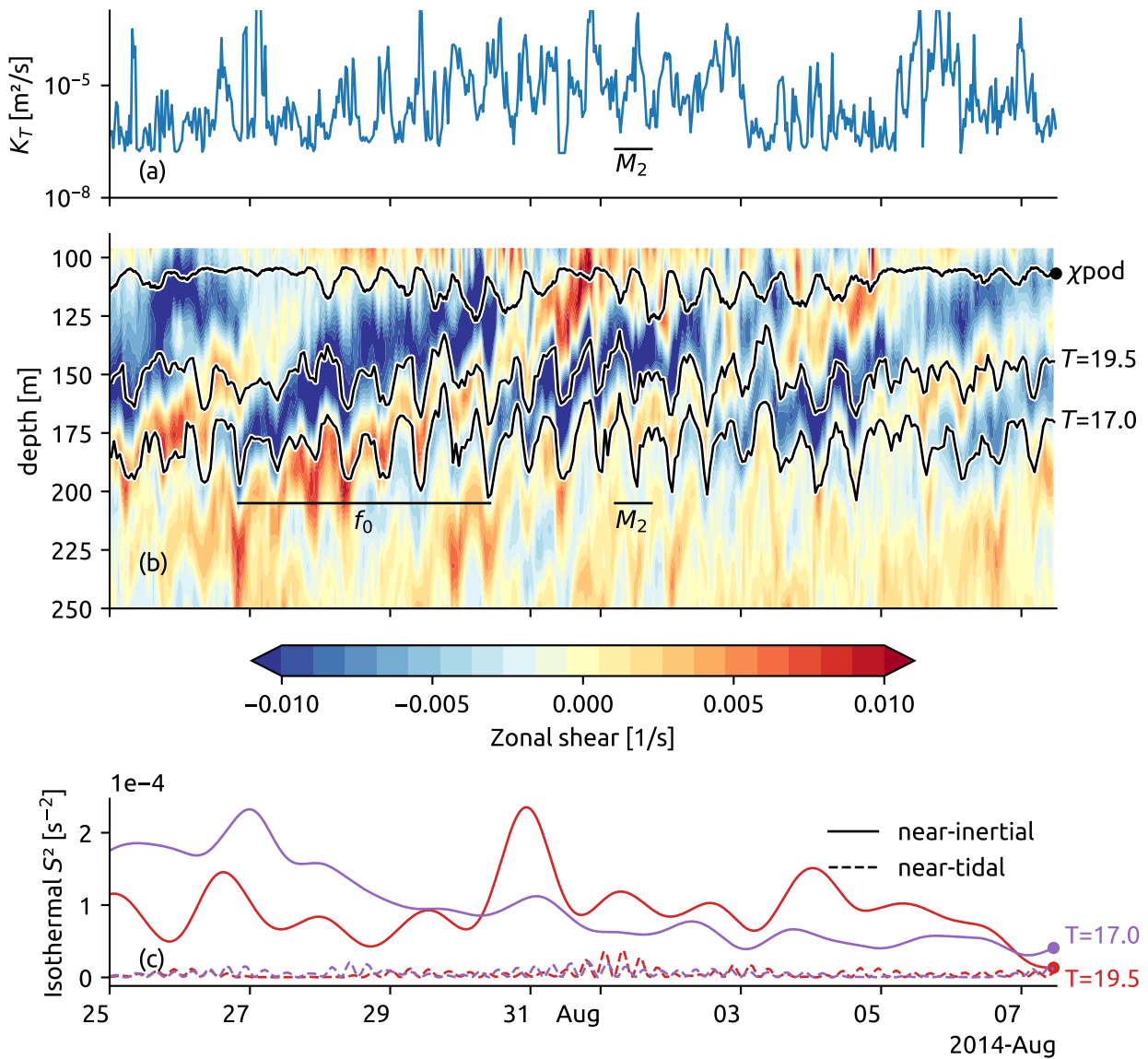


Figure C9. An example of pumping of the near-inertial shear layers past the  $\chi_{\text{pod}}$  by the  $M_2$  tide at NRL5. The time period of focus is highlighted in white in Figure C6. Time series of (a) turbulent diffusivity  $K_T$ , (b) zonal shear and (c) near-inertial and near-tidal shear on two isotherms for a period of high mixing associated with downward propagating near-inertial energy. Horizontal lines indicate the inertial period (3.79 days; labelled  $f_0$ ) and the  $M_2$  period (12.42 hours; labelled  $M_2$ ). Also shown in (b) are the depth of the  $\chi_{\text{pod}}$  and two isotherms ( $17^\circ\text{C}$ ,  $19.5^\circ\text{C}$ ). (c) Near-inertial shear dominates near-tidal shear by an order of magnitude on the two isotherms ( $17.0^\circ\text{C}$ ,  $19.5^\circ\text{C}$ ). The two time series are obtained by first interpolating total shear to isothermal space and then filtering as in Section 3.

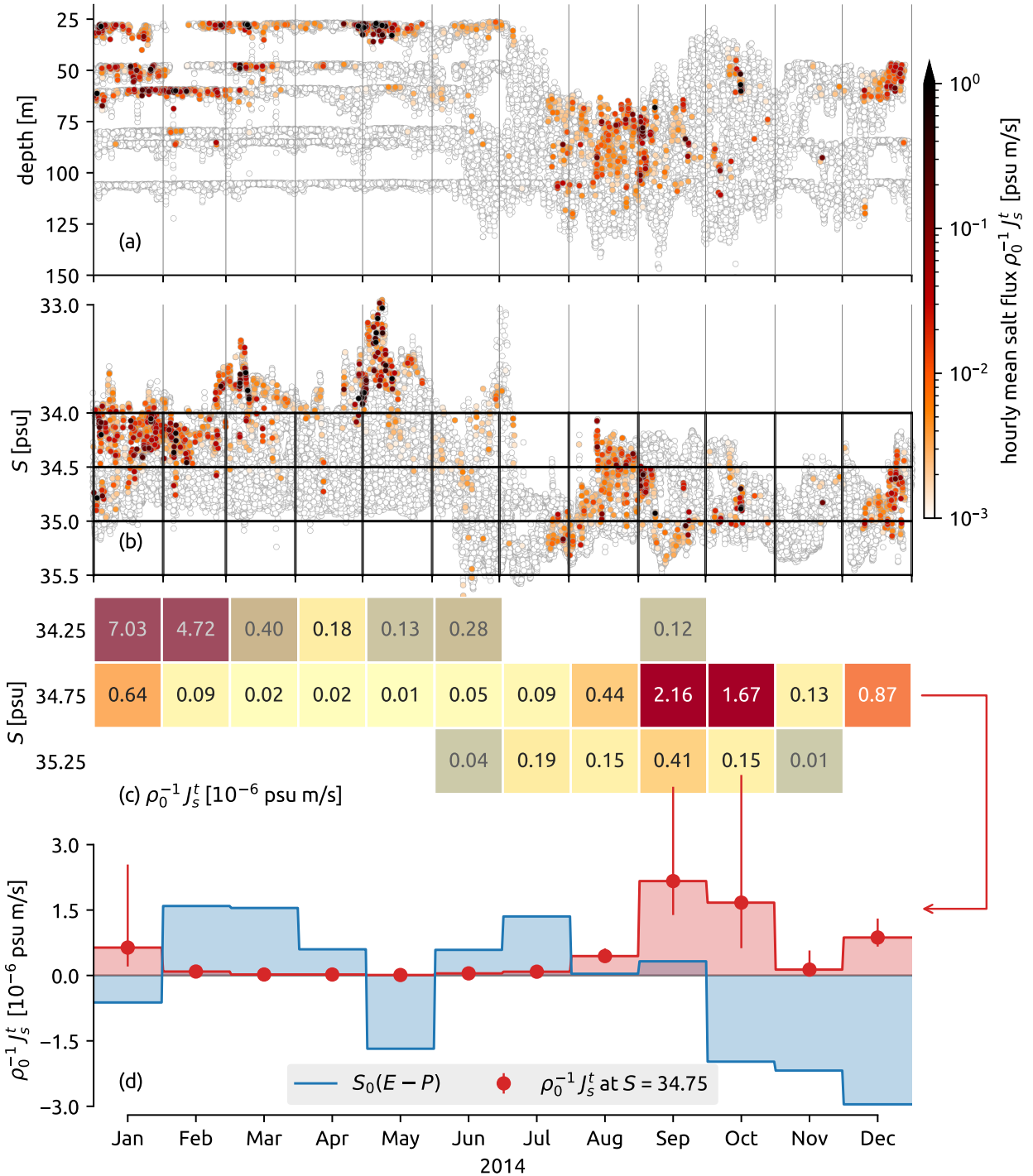


Figure C10. Annual cycle of turbulent salt flux  $J_s^t$  at 8°N. (a, b) Scatter plots of hourly averaged  $J_s^t$  in depth and salinity spaces respectively. Points with larger  $J_s^t$  are plotted over points with lower  $J_s^t$  so that high flux events are prominent. (c) Monthly averaged turbulent  $J_s^t$  through salinity surfaces  $S = 34.25, 34.75$  and  $35.5$ . These are estimated by bin averaging the values in (b) in bins with edges  $[34, 34.5, 35, 36]$ . Bins with less than one instrument-month of data are not shown. Those with less than two instrument months of data are grayed out. (d) Monthly averaged surface salinity flux  $S_0(E - P)$  estimated using evaporation from OAFflux and precipitation from TRMM.  $S_0$  is assumed to be 32. In orange is  $J_s^t$  through  $S = 34.75$  from (c) with bootstrap error bars.